Numerical Analysis of Combustion of the Exhaust Gas of a Solid Oxide Fuel Cell

BY

DANIELE BONGIOVANNI
Laurea, Politecnico di Torino, Turin, Italy, 2012

THESIS

Submitted as partial fulfillment of the requirements
for the degree of Master of Science in Mechanical Engineering
in the Graduate College of the
University of Illinois at Chicago, 2014

Chicago, Illinois

Defense Committee:

Suresh K. Aggarwal, Chair and Advisor
Kenneth Brezinsky
Massimo Santarelli, Politecnico di Torino

This thesis is dedicated to my family.

ACKNOWLEDGMENTS

First and foremost, I would like to thank my advisor Prof. Suresh K. Aggarwal, for his guidance throughout this work. Without his constant support it would have been impossible for me to accomplish my research goals. My deepest gratitude goes also to my advisor at Politecnico di Torino, Prof. Massimo Santarelli, who gave me the possibility to undertake this research work at UIC. I take this opportunity to express my gratitude to Dr. Viswanath R. Katta for the assistance while working with the multidimensional CFD code. A special thanks goes to my laboratory mates of the Flow and Combustion Simulation Laboratory, in particular Salvatore Quattrocchi and Xiao Fu, for the help they gave me during my year in Chicago. Eventually, I want to thank from the bottom of my heart my family and my friends for the unwavering support they always gave me during this experience in the United States.

D B

TABLE OF CONTENTS

TABLE OF CONTENTS (Continued)

CHAPTER **PAGE**

LIST OF TABLES

LIST OF FIGURES

LIST OF FIGURES (Continued)

LIST OF FIGURES (Continued)

LIST OF FIGURES (Continued)

SUMMARY

As the energy demand and the pollution concerns continue to grow, new sources of energy and environmental friendly power generation systems are being developed. In this context, syngas is considered as an attractive fuel, as it can be produced from a broad range of fossil fuel and biomass sources, including agriculture and municipal waste, using gasification processes. It is mainly composed of H_2 and CO, along with varying amounts of N_2, CO_2, and H_2O [1].

In the following work a comprehensive study about a low-energy-content fuel, presenting the characteristic components of syngas, is developed. This fuel differs from common syngas in the relative ratios between the species of the mixture; in the reported case the presence of H2 and CO is largely reduced. The present research deals with the combustion of the exhaust gas of a solid oxide fuel cell [2]. The exhaust stream from the SOFC stack, fed with biogas, contains CO_2, H_2O and some trace amount of H_2 and CO resulting from incomplete utilization of fuel in the SOFC stack. Consequently exhaust anodic fuel can be combusted with depleted air leaving the cathodic compartments of the stack, with the aim of exploiting its retained energy content and enhance the global efficiency of the system. This combustion process, however, generates several undesirable compounds, especially NO_X. Modifying of the combustion atmosphere, a change from air to oxy-combustion, allows elimination of nitrogen oxides. Recently, oxygen-enriched combustion is obtaining greater acceptance, in fact its potential value in terms of both improved heat transfer and reduction of NO_X can overcome the cost penalty of burning a fuel in a oxidizer other than air [3]. For these reasons, both pure oxygen and air solutions are covered.

SUMMARY (Continued)

An extensive investigation of the considered mixture is provided, beginning with equilibrium calculation as a preliminary analysis, continuing with opposed flow flame simulations, that allow a better understanding about the suitable combustion temperatures, the production of pollutant compounds, the influence of strain rate on the diffusion flame and the flammability limits.

In the second part of the thesis, the main focus shifts towards the development of a detailed study about the extinction behavior of syngas fuels. For this matter, a common syngas mixture (50% H_2 - 50% CO) is employed as fuel for counterflow flames. Multidimensional simulations are carried out using an advance software for unsteady reacting flows. Studies about extinction limits, blow off extinction and effects related to scalar dissipation rate have been extensively covered in the present thesis as principal objective of this part. Differences and analogies between one- and two-dimensional simulations outputs are reported and discussed, introducing an interesting field of research.

CHAPTER 1

INTRODUCTION

1.1 Motivations and Aims

Increasing concerns about climate change and depletion of energy sources are providing impetus for developing more efficient and environmental friendly power generation systems. Many concerns about the exhaust gas originated by thermo-chemical processes have been heavily addressed with great emphasis about the issues deriving from the emission of pollutant compounds. At the same time, if properly exploited, the waste gas can provide a decisive mean for enhancing the overall efficiency of a power system. In recent years, solid oxide fuel cells (SOFCs) are emerging as viable power generation systems. In addition to their high electrical efficiency (40%-60%), such devices allow the implementation of an exhaust gas burner, providing a better overall performance of the system and a reduction in the amount of emitted pollutants. The main objective of this thesis is to study how the combustion of the low-energy exhaust gas from a SOFC stack, may represent a suitable way to recover part of the waste energy and thus enhance the system efficiency [4]. The target fuel of this research is the exhaust gas of a solid oxide fuel cell, a gas mixture similar in composition to that of syngas, but significantly reduced in CO and H_2 content. In order to investigate the feasibility of utilizing this fuel in common combustion devices, numerical simulations of different kinds of flame are performed so that a good modeling of the problem and realistic results can be obtained. In order to satisfy

the American and Kyoto protocol's environmental restrictions, special attention is also paid to the emissions of pollutants, especially NO_X.

The present work represents an extension of a study that has been performed through the European project, SOFCOM [2]. This research focuses on the study of the performances of several fuel cells. In recent years, extensive analyses have been performed about the recovery of energy from the exhaust gases of fuel cells, in order to enhance the overall performance of the system and reduce emissions. Following this path, in this research all the data regarding composition of the gas and initial conditions are extracted from this project.

The general analysis of the exhaust gas starts with preliminary equilibrium calculations for different gas compositions and equivalence ratios. As good representation of a wide range of applications, laminar diffusion flames are analyzed. Influence of oxidizer composition and fuel inlet temperature and flammability boundaries are evaluated to show the ability of exploiting the heat released by the fuel, combined with a reduced emission of pollution. Particular attention is paid to the extinction behavior of the employed fuel; to do so, a two-dimensional software is also used to display the characteristics of the counterflow flame [5].

Along with the study of the combustion of the low-energy fuel, the research examines the extinction behavior of syngas diffusion flames in a opposed-jet configuration. Such investigation is important from fundamental aspects, as few studies have been performed on syngas fuels, and most of all it would give solid information about the best conditions to employ the fuel avoiding the occurrence of extinction. In the present research, simulations are carried out using both one- and two-dimensional CFD codes: CHEMKIN [6] and UNICORN [7] [8], respectively.

From the simulation results, a detailed investigation of the extinction behavior of syngas flames has been performed. A syngas mixture with 50% H_2 and 50% CO has been considered.

Another objective is to examine the validity of one-dimensional approximation for counterflow flames by comparing the results of 1-D and 2-D simulations. Both stretch-induced and dilution-induced extinction characteristics are investigated, paying special attention to the evolution of the scalar dissipation rate. As a matter of fact, one of the purposes of the analysis is to exploit the information coming from the study of the mixture fraction and the scalar dissipation rate in order to effectively describe the extinction characteristics of counterflow flames. These parameters become indeed very useful when describing nonequilibrium phenomena like the extinction of a flame. A demonstration of the ability to predict the location and the condition in which the flame starts to extinguish is searched for several configurations.

1.2 Syngas Background

The term syngas is a blend word that comes from the union of the words, synthetic gas. It doesn't indicate a pure gas, but a mixture of gases, mainly carbon monoxide and hydrogen, along with varying amounts of methane, carbon dioxide and water. The specific composition depends on the kind of source and the production method. In general, syngas has superior combustion and emission characteristics compared to the original feedstock such as biomass, coal or solid waste. Some examples of production methods are gasification of coal, biomass and solid waste, and steam reforming of natural gas and liquid hydrocarbons [1].

Syngas also has significant advantages with respect to the traditional fuels. In particular, the presence of hydrogen in syngas allows improvement in combustion performance, reduction

in emissions, and extension of flammability limit. For these reasons, syngas is expected to be one of the most promising fuels in future energy production [9].

1.3 Description of the SOFC System

Since the investigated fuel is the exhaust gas from a solid oxide fuel cell, an overview of the SOFC system is provided in this section. Figure 1 presents a schematic of a conventional system with post combustion of exhaust gas using air as oxidizer. The main components include the SOFC stack, fuel and air delivery lines, and burner located downstream of the fuel cell stack.

The system is fed by biogas (60% CH_4 and 40% CO) which undergoes complete external steam reforming. In the analyzed configuration no external water stream was used to generate hydrogen-rich gas via steam reforming. For that reason, to maintain proper steam to the carbon ratio, fraction of anode off-gas was recirculated. Steam reforming is done recovering the H_2O from the outlet of the SOFC. The balance of H_2O is closed, so the recovered H_2O is sufficient. The fraction of exhaust gas used for steam reforming has to be minimized, and it is usually equal to 60%-70% of the anode exhaust.

The composition (mole fraction) of the reformed fuel is indicatively the following: 50% H_2, 20% CO, 20% H_2O, 10% CO_2. The syngas stream enters anode side of SOFC stack with a temperature equals 800°C. Air is supplied to the cathodic compartments of the stack at temperature of 650°C.

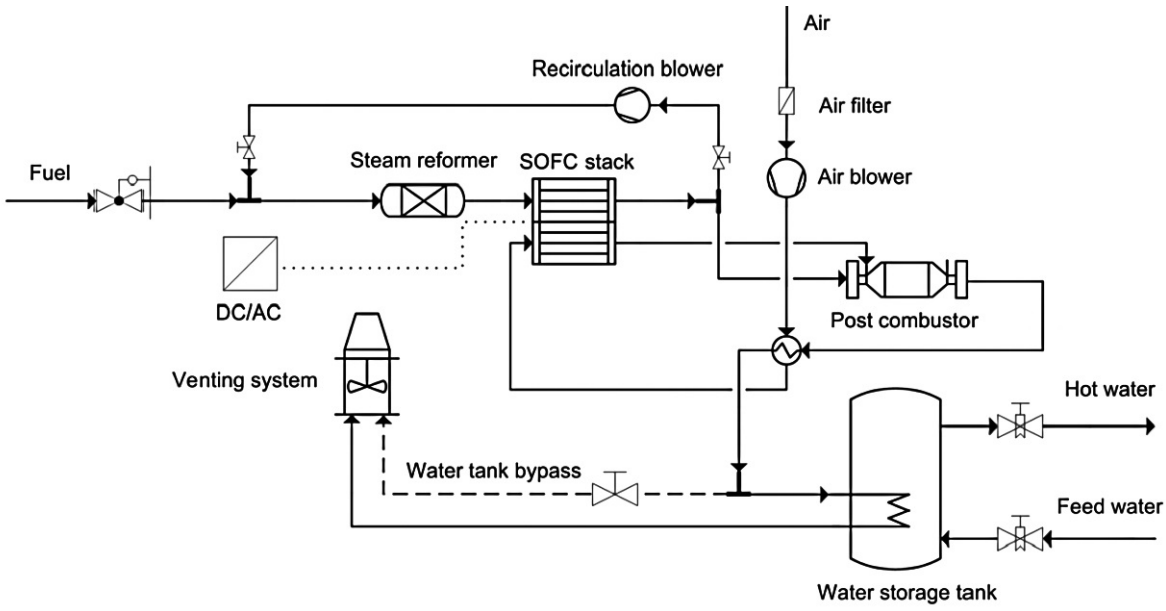

Figure 1: Scheme of SOFC-based system with the flame burner.

1.3.1 Solid Oxide Fuel Cell Overview

Solid oxide fuel cells (SOFCs) are devices used to generate electricity at high efficiencies and low pollutant emissions. They convert chemical energy of fuels into electrical energy directly without the common thermodynamic restrictions of heat engines. Moreover these devices provide many advantages over traditional energy conversion systems including high kinetics of both chemical and electrochemical reactants, reliability, modularity, fuel adaptability, lack of precious catalysts and very low levels of polluting emissions. The main disadvantage is the high operating temperature that produces some additional issues, such as long start-up times [10].

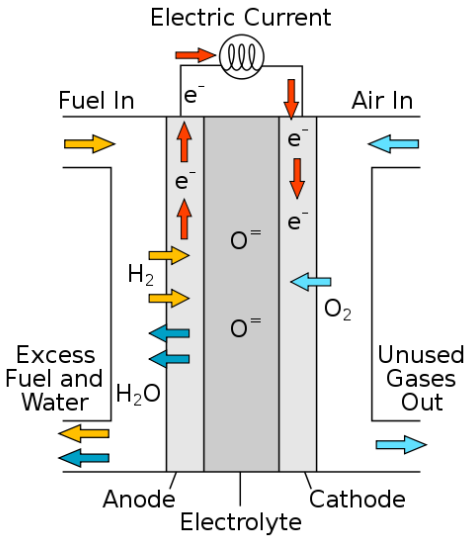

Figure 2: Schematic diagram of the structure of a SOFC.

A SOFC (Figure 2) is composed of two porous electrodes. The electrodes are separated by an electrolyte, which allows the flowing of oxide ions. Air flowing along the cathode supplies oxygen that reacts with the electrons coming from the external circuit. This forms oxygen ions, which migrate to the anode side of the fuel cell (through the electrolyte). At the anode, oxygen ions react catalytically with the fuel, producing water, carbon dioxide, heat, and electrons. The electrons flow from the anode through the external circuit to the cathode [11]. The global reactions involved in the energy conversion process are the following.

Cathode side:

$$O_2 + 4e^- \rightleftharpoons 2O^{2-} \tag{1.1}$$

Anode side:

$$H_2 + O^{2-} \rightleftharpoons H_2O + 2e^- \tag{1.2}$$

$$CO + O^{2-} \rightleftharpoons CO_2 + 2e^- \tag{1.3}$$

Several kinds of fuel can be employed in a solid oxide fuel cells, including hydrocarbon fuels. These systems operate at relatively high temperatures, between 900°C and 1000°C, allowing highly efficient conversion to power and internal reforming. Recently, planar SOFCs operating at lower temperatures (700°C to 850°C) have been investigated. Lower temperatures would help lower the cost since less-expensive materials may be used [12].

1.3.2 Post Combustor Overview

The exhaust gas from the SOFC, is mostly composed of CO_2 and H_2O. However, due to incomplete transformation inside the fuel cell, it also contains a significant amount of CO and H_2. In order to recover part of the energy in this gas, a post combustor is installed downstream the SOFC stack. Inside the combustion chamber, the gas undergoes chemical reactions producing thermal energy, carbon dioxide and water. Such a post combustion device also becomes even more important for reduction of carbon footprint. Concept of integrating SOFC-system with combustion process is becoming popular for conventional power generators [13]. In addition, reduction of the amount of generated greenhouse gases can be achieved by separation of CO_2 stream from the exhaust. In the analyzed SOFC-based system, combustion process of the spent anodic fuel in high purity oxygen and air atmospheres generates CO_2-rich flue gas which is sent to the carbon capture and sequestration section.

1.4 Fuel Characteristics

Referring to the SOFCOM project [2], all the useful data related to the fuel are reported below. The composition of the exhaust mixture exiting the fuel cell is summarized in Table I. The lower heating value (LHV) of the mixture is equal to 1972.55 kJ/kg.

TABLE I: FUEL COMPOSITION EXPRESSED IN TERMS OF PERCENTAGE MOLE FRACTIONS

Chemical Species	**% Mole Fractions**
CO_2	23.96
CO	5.45
H_2	12.2
H_2O	58.39

The exhaust gas leaves the SOFC stack with a temperature in the range of 700°C - 800°C and is then fed into the combustor, where the mixture is burned. As suggested in the SOFCOM project, computations are performed for mixture temperatures of 700 and 970°C (Table II), representing two typical situations. The temperature of 700°C represents conditions at the exit of the SOFC stack, while in the second case, as suggested in the SOFCOM project [2], the mixture is heated to improve the mixture flammability and combustion performance. The oxidizer stream contains O_2 and N_2, but the O_2 mole fraction is varied.

TABLE II: FUEL AND OXIDIZER INITIAL CONDITIONS

Case #	**T fuel** [°C]	**T oxidizer** [°C]
1	700	20
2	970	20

CHAPTER 2

FUEL CHEMICAL EQUILIBRIUM

2.1 Introduction

Chemical equilibrium calculations are fundamental to evaluate the principal thermodynamic properties of a combustion system. A general analysis of the performances of the burning fuel for different conditions is useful to assess the quality of such set up and can provide a rough estimate of the pollutants emissions. Different initial conditions are simulated, with a particular interest in the variation of thermodynamic and chemical properties with equivalence ratio. The CHEMKIN software (Release 10113) developed at Reaction Design [6] [14] was used to perform equilibrium simulations.

2.2 CHEMKIN Overview

CHEMKIN is a commercial software, which is used to solve complex chemical kinetics problems. Mostly employed in the field of microelectronics, in the automotive sector for combustion processes and in the chemical processing industry, it has become an important tool to explore potential design solutions before expensive hardware is manufactured. It is written in Fortran and consists of two Fortran blocks (the interpreter and the gas-phase subroutine library) and a thermodynamic database. It is composed of several programs and subroutine libraries, which working together enable the simulation of complex chemical reactions.

2.3 Chemical Kinetic Mechanisms

As part of the inputs, CHEMKIN requires a reaction mechanism, which describes the overall chemical reaction through a sequence of elementary reactions. "It describes each reactive intermediate, activated complex, and transition state, and which bonds are broken, and which bonds are formed. Reaction intermediates are chemical species, often unstable and short-lived, which are not reactants or products of the overall chemical reaction, but are temporary products and reactants in the mechanism's reaction steps. Reaction intermediates are often free radicals or ions. Transition states can be unstable intermediate molecular states even in the elementary reactions. Transition states are commonly molecular entities involving an unstable number of bonds and unstable geometry. They correspond to maxima on the reaction coordinate, and to saddle points on the potential energy surface for the reaction" [15].

All this information is stored in three data files that together form the reaction mechanism: gas-phase kinetics file, thermodynamics data file and gas transport data file.

2.3.1 San Diego Mechanism

Among the various detailed mechanisms that are available in the literature, the San Diego mechanism [16] has been used to model the syngas oxidation in this work. The mechanism has been validated previously against a variety of targets including ignition delays, flame velocities, structures and extinction characteristics. It is composed of 48 species and 244 reversible reactions. The standard mechanism does not include the nitrogen chemistry. For the present study, the NO_X chemistry was added to the basic mechanism, with the resulting mechanism containing 61 species and 297 reversible reactions.

2.3.2 Syngas Experimental Validation

Figure 3 present an experimental validation for syngas fuel [17]. Figure 3(a) plots the measured and predicted temperature profiles. Diffusion flames are simulated employing a syngas mixture (50% CO - 50% H_2) as fuel and air as oxidizer. Initial parameters are summarized in Table III.

TABLE III: COUNTERFLOW FLAME'S INITIAL PARAMETERS

Composition	**Pressure**	**Strain Rate**	**Inlet velocity**		**Initial temperature**	
			Fuel	**Oxidizer**	**Fuel**	**Oxidizer**
50% CO - 50% H_2	1 atm	35 s^{-1}	13.84 cm/s	13.84 cm/s	300 K	300 K

Experimental results are corrected so that the effect of radiations are taken into account. Simulations are performed using four mechanisms: San Diego [16], Davis [18], AramcoMech 1.3 [19] and GRI 3.0 [20]. The peak temperature predicted by the different mechanisms show good agreement between each other and with the experimental measurements. The reported location of the peak is instead different from the experimental results. The experimental peak is shifted by 0.18 cm towards the oxidizer nozzle, which is due to the suction for depletion of excess fuel [17] [21].

In addition, results for laminar flame speed are also reported. In this case premixed syngas-air mixtures are simulated and measured. Pressure is fixed and equal to 1 atm. Two syngas

mixture are considered. Figure 3(b) plots the influence of the equivalence ratio on the laminar burning velocity for two flames, differing in employed syngas mixture. The first one uses a mixture of 50% CO and 50% H_2 as fuel, while the second 95% CO and 5% H_2.

For the first flame, San Diego and Davis mechanisms simulated results are close to the experimental measurements. A small error occurs in the prediction of the peak values, where these mechanisms show a minimal overprediction. The GRI 3.0 mechanism results are not as good as the others, presenting a significant deviation, especially in the evaluation of the peaks.

From this analysis, the second flame is simulated using only Davis and San Diego, which showed the best agreement. Here the predicted values present a very close agreement with the measurements. The flammability limits extend from $\phi = 0.7$ to $\phi = 5.5$, for all the employed mechanisms and for both the flames considered. For the first flame, the peak in laminar burning velocity is achieved for $\phi = 2.0$, while for the second flame the peak is located at $\phi = 2.5$.

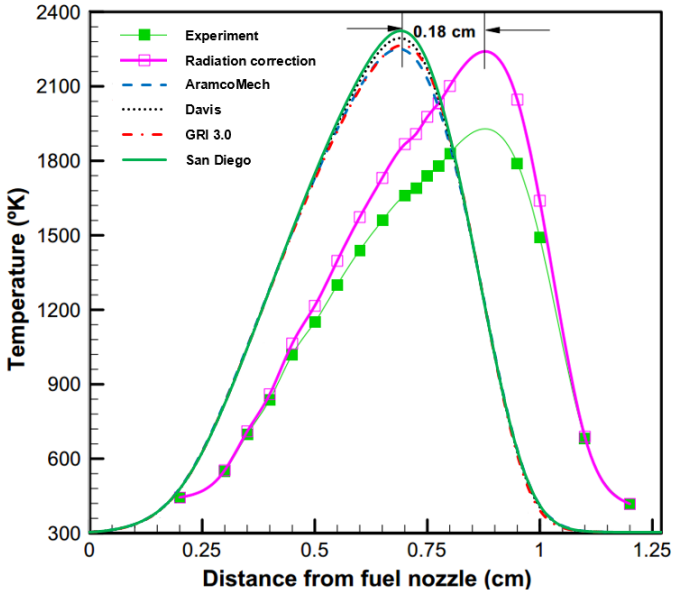

(a)

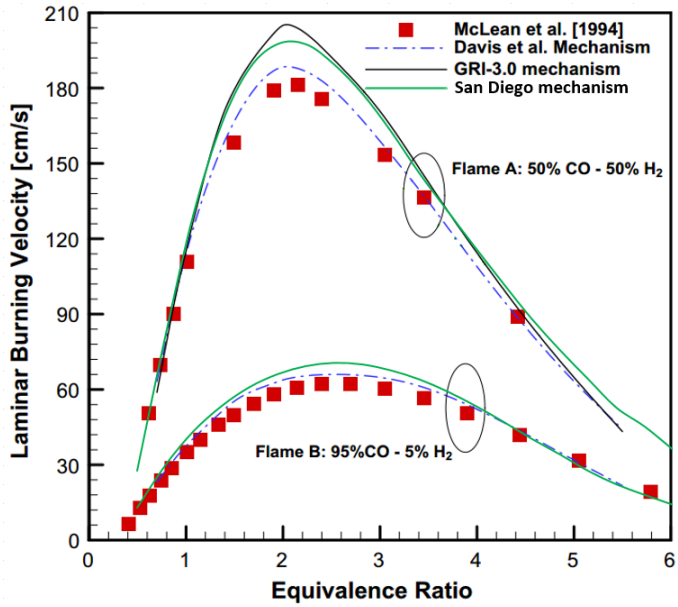

(b)

Figure 3: Syngas experimental validation. Counterflow flame structure (strain rate = $35s^{-1}$) and laminar flame speed versus equivalence ratio (Flame A: 50% CO - 50% H_2, Flame B: 95% CO - 5% H_2).

2.4 Physics of Chemical Equilibrium

Chemical equilibrium study is useful since it provides fundamental information about basic combustion processes associated with a combustible mixture. It yields the equilibrium temperature and composition of the mixture, including minor species.

Two adiabatic flame temperatures can be defined, corresponding to constant-pressure and constant-volume conditions. For this study, constant pressure combustion is considered. When a mixture of fuel and air burns adiabatically at constant pressure, the absolute enthalpy of the reacting compounds at the initial condition (e.g., $T = 298$ K, $P = 1$ atm) is equal to the absolute enthalpy of the products at the final stage (e.g., $T = T_{ad}$, $P = 1$ atm). Therefore the following relationship is valid:

$$H_{react}(T_i, P) = H_{prod}(T_{ad}, P) \tag{2.1}$$

Here H_{react} is the enthalpy of reactants and H_{prod} is the enthalpy of products [22]. The equilibrium composition is determined from the minimization of the Gibbs free energy function [23].

2.5 Determination of Chemical Equilibrium with CHEMKIN

The following section is extracted from CHEMKIN Manual [24].

> In addition to chemically reacting flow applications, CHEMKIN includes an Equilibrium Reactor model. This model allows users to determine the chemical state of a mixture under equilibrium conditions. Any number of gas-phase or condensed

species can be included in an equilibrium calculation, while surface site species are ignored. In this way, the Equilibrium Reactor model can be used to determine phase equilibrium, between gas and condensed phases, as well as chemical equilibrium. All that is required is thermodynamic data for all species in each phase.

An established method for evaluating chemical equilibrium is the element-potential method embodied in the Stanford software STANJAN [25]. The CHEMKIN Equilibrium Reactor employs the STANJAN library of routines in its solution method. The equilibrium determines composition equilibrium and phase equilibrium. The results depend only on the thermodynamic properties of the species in the user's chemistry set, as well as the starting composition and conditions specified. The starting composition determines the relative amount of chemical elements in the system. An initial estimate of the equilibrium temperature can sometimes be used to select a burned equilibrium state from an unburned equilibrium state in the case where two equilibrium states are possible.

The equilibrium program assumes that the gas-phase is a mixture of ideal gases and that condensed phases are ideal solutions. The user selects atomic populations through identity of initial species and their fraction in each phase, as well as the state parameters.

The user may specify the state parameters in a number of different ways, including

- temperature and pressure;

- pressure and entropy;
- enthalpy and pressure;
- volume and entropy.

Species composition can be frozen in a given calculation, or the equilibrium composition can be determined. Calculations may be linked through continuations, such that the conditions calculated from a previous equilibrium case can be used as the starting point for a subsequent case with different constraints. In this way, the user can employ the Equilibrium Reactor Model to analyze stages in a thermodynamic cycle.

The Equilibrium Reactor Model is also commonly used to determine adiabatic flame temperatures for combustible gas mixtures. Such a simulation is performed by specifying an initial (reagent) gas mixture and constraining equilibrium for constant enthalpy (adiabatic) and constant pressure. The calculation can also be performed using constant internal energy and constant volume. An initial guess for the equilibrium temperature of $\sim$1000 K or above is usually needed to cause the equilibrium solver to find the burned-gas solution. For accurate adiabatic flame temperature calculations, it is important to include all radical species that might occur in the flame, as well as stable reactants and products.

The following sections summarize the equations solved and the methodology used for determining chemical and phase equilibria of arbitrary systems. [24]

2.5.1 Gibb's Free Energy Minimization

The following section is extracted from CHEMKIN Manual [24].

The basic theory for the element-potential method of determining equilibrium is based on the minimization of Gibb's free energy. The Gibb's function of a system is:

$$G = \sum_{k=1}^{K} \bar{g_k} N_k \tag{2.2}$$

where $\bar{g_k}$ is the partial molal Gibb's function and N_k is the number of moles of each k species in the system. K is the total number of species.

For ideal-gas mixtures or ideal solutions, the partial molal Gibb's functions are given by:

$$\bar{g_k} = g_k(T, P) + RT \ln X_k \tag{2.3}$$

where $g_k(T, P)$ is the Gibb's function for the pure species k, evaluated at the system temperature and pressure; R is the universal gas constant; and X_k is the mole fraction of the kth species.

The equilibrium solution at a given temperature and pressure is the distribution of N_k that minimizes the system Gibb's function, G, subject to atomic population constraints (and non-negative N_k). The atomic population constraints are:

$$\sum_{k=1}^{K} n_{jk} N_k = p_j \qquad j = 1, ..., M \tag{2.4}$$

where n_{jk} is the number of the jth atoms that appear in the kth molecule, is the total population in moles of the$j$th atom in the system, and M is the total number of different elements that are present in the system.

Details regarding the relationship between the partial molar Gibb's functions and the elemental potentials for the atoms, as well as the explicit form of the equations solved in the STANJAN library, are described in the STANJAN report [25]. [24]

2.6 Set Up an Equilibrium Calculation with CHEMKIN

CHEMKIN is a user-friendly software, in which all input data are set through a graphical interface and no programming or terminal commands are needed to correctly set up a simulation. The configuration of an equilibrium calculation starts from the creation of a project file where all the simulation parameters are stored. CHEMKIN provides several models of reactors, each one useful to study a specific application. They are collected in the models window, where the user should specify the type of simulation he is willing to carry out. In this case, one selects the icon of Equilibrium Reactor Model. To properly perform the simulation, CHEMKIN requires the selection of the chemical kinetic mechanism, specified inside the pre-processing window. Here the user should select the working directory and enter the Gas-Phase Kinetics File, the Thermodynamics Data File and the Gas Transport Data File (even though the last one is not necessary for equilibrium calculation, it will be useful for other types of simulation). These files are provided by the developers of the respective mechanisms and sometimes can be expanded if more species and chemical reactions have to be taken into account. In this study most of the simulations employ the San Diego Mechanism developed by University of California [16].

After this, the user should define all the physical and chemical inputs: initial temperature and pressure of the mixture, involved reactant species, in mole or mass fraction, specifying the equivalence ratio if desired. Constraints can be also entered if necessary. The type of physical problem has to be defined too; in this case, the Constant Pressure Enthalpy is chosen. After this, the simulation is run and, once completed, the user is allowed to post-process the outputs, in particular CHEMKIN provides the possibility to export the data to an Excel sheet.

2.7 Simulation Results

For this preliminary investigation, different conditions are simulated. Firstly the most feasible set up is considered: the exhaust of the fuel cell is at 700°C (973.15 K) and the air is at room temperature (293.15 K). Since an initial temperature of the mixture is required as an input, a weighted average between fuel and oxidizer temperatures is employed. In this first case, considering stoichiometric conditions ($\phi = 1$), the initial temperature is equal to 820.15 K and the pressure is 1 atm. At the equilibrium, a temperature of 1593.8 K is achieved. Comparing this value with the maximum temperature reached in an identical configuration, using a common syngas mixture (i.e., using 50% H_2 and 50% CO, flame temperatures higher than 2000 K are easily achievable), the difference is relatively large. This fact is due to the dilution of the studied fuel mixture.

As suggested by the SOFCOM project, raising the temperature of the fuel could enhance combustion performance in terms of efficiency and mixture flammability. Hence, the fuel temperature is set to 970°C (1243.15 K), whereas the air is kept at room temperature. The weighted average temperature is now 1029.4 K, the pressure equal to 1 atm. The computed equilibrium

temperature at $\phi = 1$ is 1767 K. The higher temperature is a direct consequence of the higher initial temperature. Table IV provides the equilibrium mixture composition in terms of mole fractions for the two temperature cases.

TABLE IV: EQUILIBRIUM COMPOSITION MOLE FRACTIONS OF CHEMICAL SPECIES INVOLVED IN THE COMBUSTION PROCESS

Chemical Species	**Initial State**	**Equilibrium State**	
		Case 1	**Case 2**
N_2	0.2338	0.2492	0.2489
H	0	$7.61 \cdot 10^{-7}$	$7.36 \cdot 10^{-6}$
O_2	0.0621	0.00021	0.00079
OH	0	$7.94 \cdot 10^{-5}$	$3.61 \cdot 10^{-4}$
O	0	$1.97 \cdot 10^{-7}$	$2.48 \cdot 10^{-6}$
H_2	0.0859	0.00022	0.00074
H_2O	0.4111	0.52955	0.52848
CO	0.0384	$2.77 \cdot 10^{-4}$	$1.14 \cdot 10^{-3}$
CO_2	0.1687	0.22046	0.21943
NO	0	$3.39 \cdot 10^{-5}$	$1.28 \cdot 10^{-4}$
NO_2	0	$4.44 \cdot 10^{-9}$	$2.12 \cdot 10^{-8}$

During the combustion process H_2 and CO are consumed through the following global reactions:

$$H_2 + \frac{1}{2}O_2 \rightleftharpoons H_2O \tag{2.5}$$

$$CO + \frac{1}{2}O_2 \rightleftharpoons CO_2 \tag{2.6}$$

As indicated in Table IV, both of these compounds are consumed and transformed into their corresponding products. Thanks to the analysis of the equilibrium composition, the first case appears to be the most suitable for real applications. The retained amount of fuel at the equilibrium is reduced compared to the second situation. In addition, the second case presents poor characteristics in terms of pollutant production. The increase in initial temperature has indeed caused a higher production of NO_X compounds. NO release shows an increase of 380% whereas NO_2 emission is almost five times greater in the second case.

2.7.1 Effect of Equivalence Ratio

Case 1

Figure 4 shows the effect of equivalence ratio (ϕ) on the adiabatic flame temperature and mixture composition at equilibrium. The variation of temperature with ϕ, shown in Figure 4(a), is mainly determined by its effect on mixture composition, heat of combustion, and specific heat. The peak temperature occurs at ϕ value slightly higher than 1. For leaner mixtures, the temperature is reduced due to the high content of N_2 in the mixture, whereas for richer mixtures, the temperature is lower due to dissociation effects [26]. The species profiles with respect to ϕ are shown in Figures 4(b), 4(c) and 4(d). As expected, for lean conditions, the mole fractions of O_2 and N_2 in the mixture decrease while those of H_2O and CO_2 increase as ϕ increases to the stoichiometric value. Figure 4(c) shows a rapid increase in CO mole fraction as ϕ increases for rich mixtures due to CO_2 dissociation [12].

Case 2

Analogous considerations can be done for the second case, where the initial temperature of the fuel is increased. The trends shown by temperature and by most of the species are similar to those of the first case. However, it is important to notice that the slopes of CO and H_2 curves are slightly different. The increased initial temperature leads to a flatter H_2 curve; on the contrary, the equilibrium fraction of CO increases more rapidly with the equivalence ratio. Finally, it is remarkable to underline the fact that an increase in temperature causes a higher production of NO_X pollutant compounds for lean mixtures, as shown in Figure 5(d).

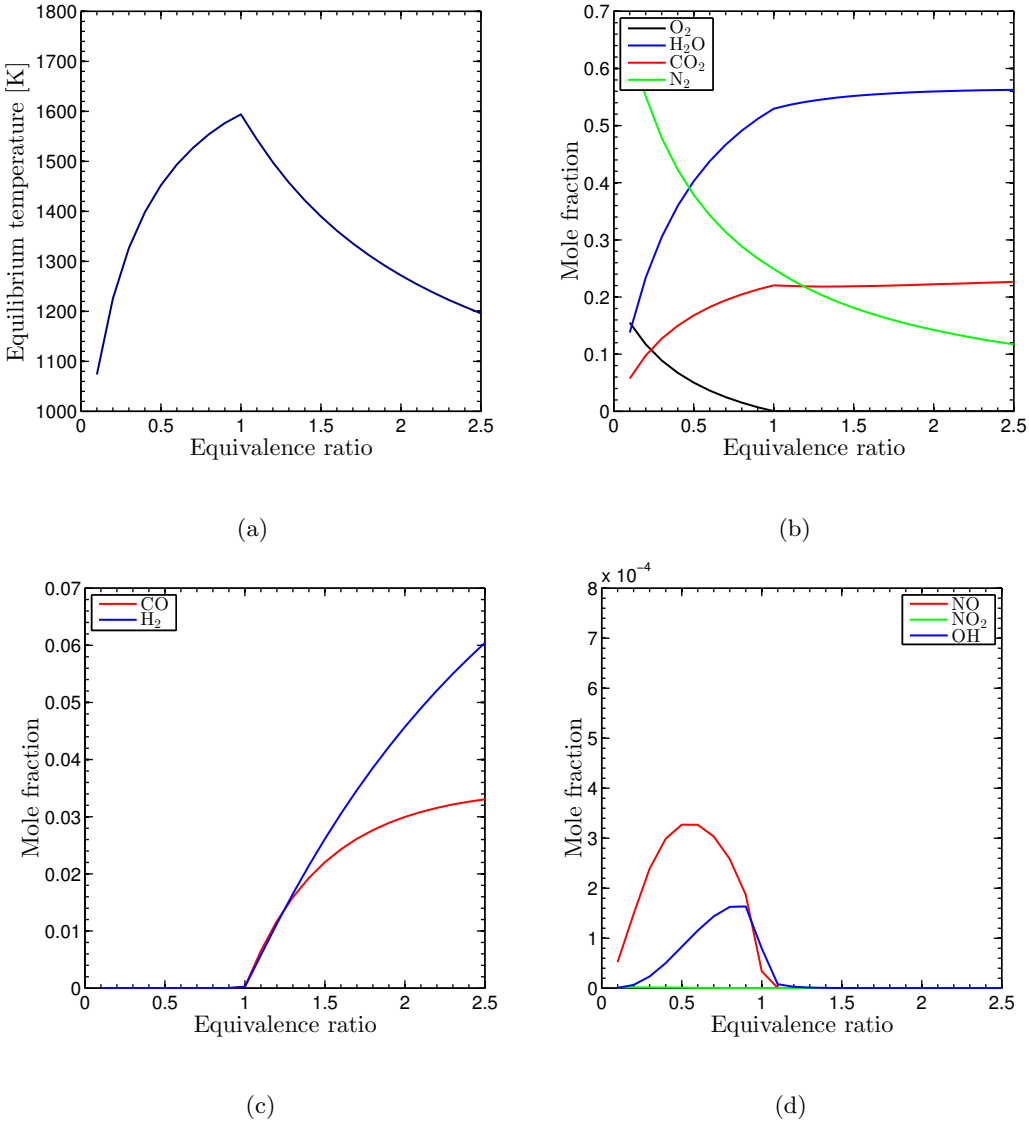

Figure 4: Effect of equivalence ratio on equilibrium temperature and product species.

Case 1: $T = 820.15$ K, $p = 1$ atm

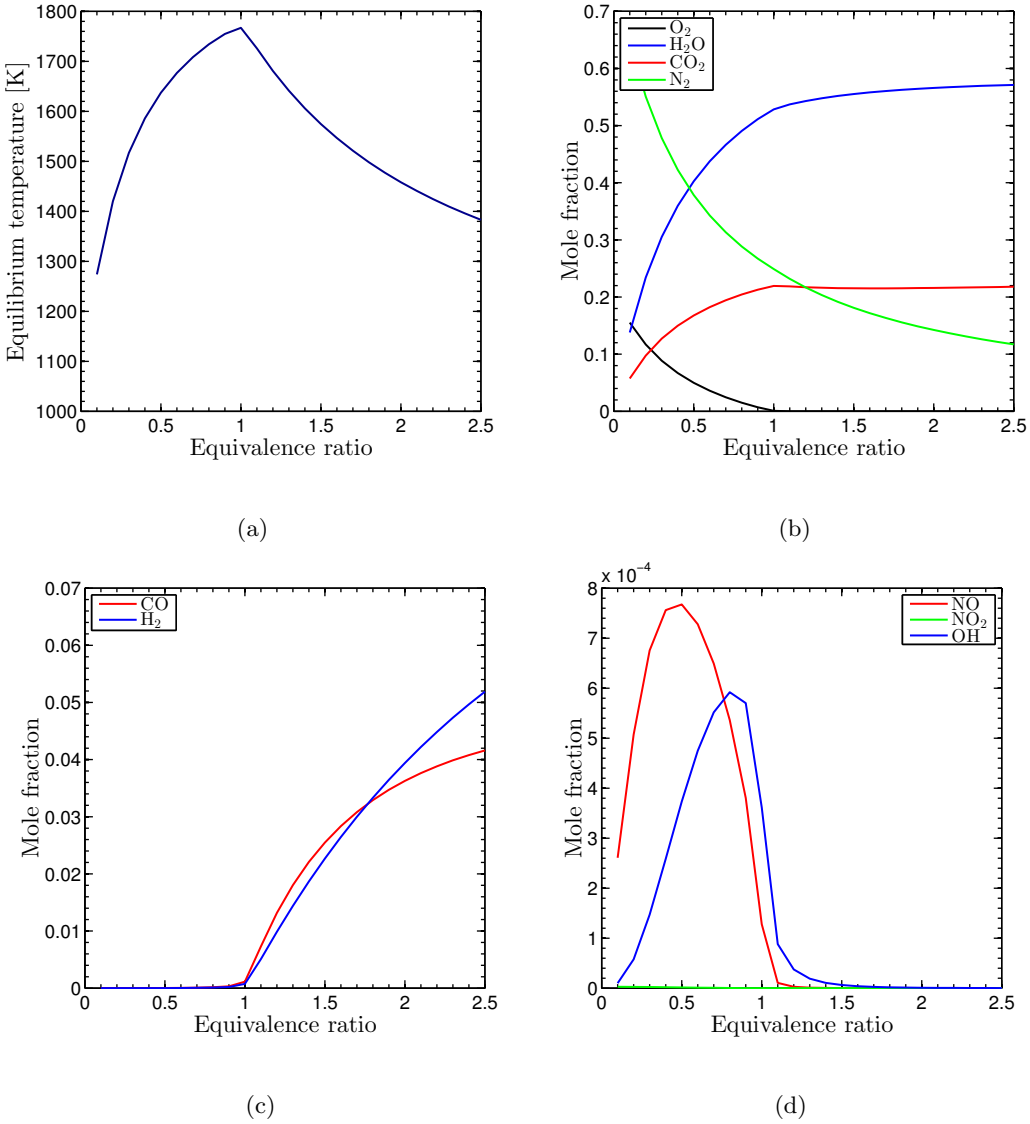

Figure 5: Effect of equivalence ratio on equilibrium temperature and product species.

Case 2: $T = 1029.4$ K, $p = 1$ atm

CHAPTER 3

PERFECTLY STIRRED REACTOR

3.1 Governing Equations

A perfectly stirred reactor is an ideal adiabatic reactor in which the volume of the reactor as well as temperature, pressure, and species composition are assumed uniform over the entire reactor. This means that there are no transient or directional effects within the reactor, and the species composition in the outlet of the reactor is the same as within the reactor. A graphical representation of the perfectly stirred reactor is given in Figure 6.

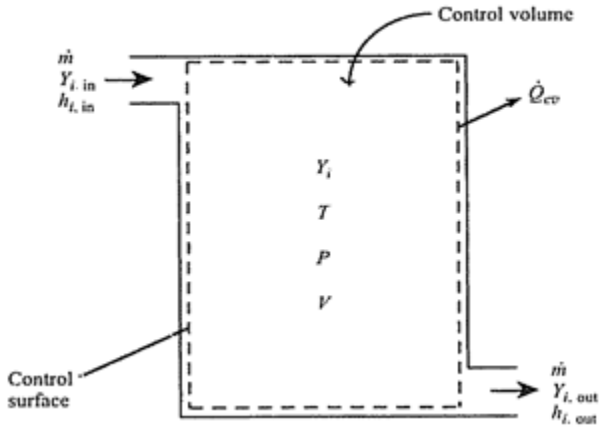

Figure 6: Perfectly stirred reactor.

Solving for temperature and species mass fraction is similar to calculation of adiabatic flame temperature, done previously in the chemical equilibrium study. The difference is that now the product composition is constrained by chemical kinetics rather than by chemical equilibrium.

3.2 Simulation Results

With both the mathematical model describing the perfectly stirred reactor as well the method of solution for the governing equations [22], the results for a syngas simulations obtained with the CHEMKIN software is now discussed. The simulations were carried out for the same syngas mixture, at stoichiometric condition. The fuel species (H_2 and CO), oxygen, the hydroxyl radical (OH), water, carbon dioxide, and temperature are plotted versus the residence time to determine at which residence time the equilibrium assumption can be considered valid, as well as to determine the blowout residence time. The temperature of the inlet mixture was 820.15 K, the reactor pressure was set to 1 atm, and the reactor volume was specified as 67.4 cm^3. The San Diego mechanism was used to obtain the results.

Figure 7 and Figure 8 contain the results obtained when the equivalence ratio was set to 1. As can be seen from the graph at a residence time of roughly 0.1 s the temperature and well as the mole fractions of the species considered are either at or very close to their equilibrium values. At a residence time of less than 0.001 s the temperature as well as the mole fractions start to noticeably deviate from their equilibrium values, and at approximately 0.145 ms blowout occurs. It is worthy of mention that the OH mole fraction deviates the least over the range of residence times varying from blowout until equilibrium composition is achieved. This is not a surprising result considering that this species is highly reactive, so once its mole fraction differs

considerably from the equilibrium values it is expected that the propagation of the reaction will be effected.

Water and carbon dioxide mole fractions, which can be considered a measure of the completeness of the reaction, decrease steadily as the residence time is decreased from the 0.01 s value with the largest changes occurring near the blowout. The temperature also follows a even more steep trend. Conversely, the oxygen, carbon monoxide and hydrogen mole fractions increase as the residence time is decreased. This also illustrates a decrease in the completeness of the reaction as more of the oxidizer, oxygen, as well as fuel, carbon monoxide, remains at the reactor outlet.

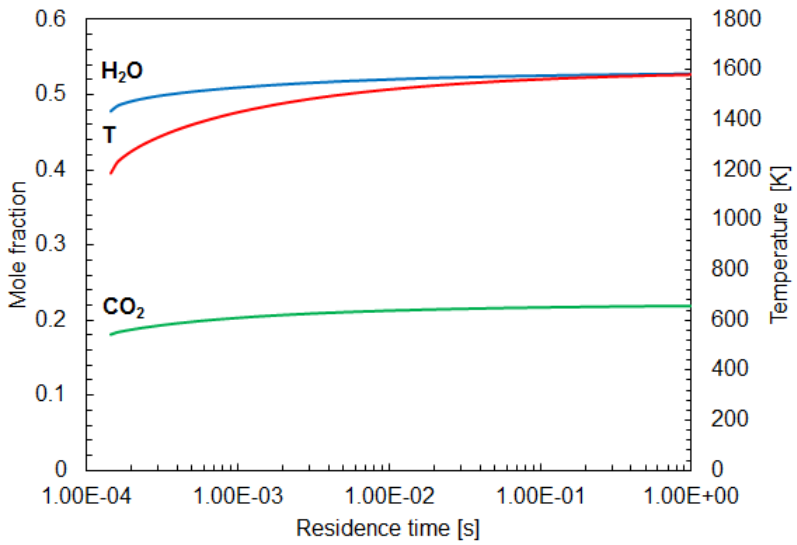

Figure 7: Mole fraction and temperature results obtained for an equivalence ratio of 1 and combustion in air.

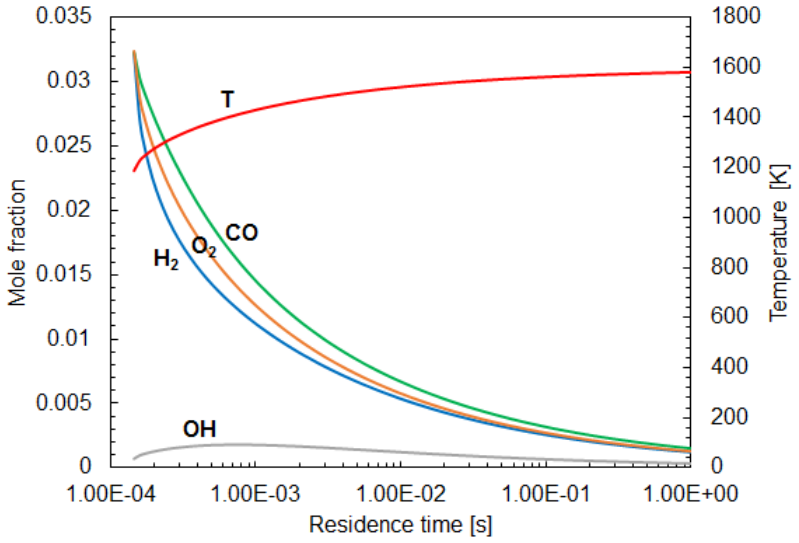

Figure 8: Mole fraction and temperature results obtained for an equivalence ratio of 1 and combustion in air.

Next, in addition to the standard combustion in air, the blowout residence times were obtained for oxidizer mixtures containing 10% O_2 and pure oxygen stream. Figure 9 contains the results obtained for the three cases.

One immediate observation is that the lower the amount of oxygen present in the oxidizer the higher the residence time required for blowout. This illustrates that at any given equivalence ratio the mixture with higher oxygen content is able to react at larger mass flow rates, or lower residence times.

This is particularly noticeable for equivalence ratio lower than 2, and becomes less so at rich equivalence ratios ($\phi > 2$) where the blowout residence times become relatively similar

regardless of the oxidizer composition. Such a result is expected as oxygen is highly reactive; hence it is not surprising that when the oxidizer contains more oxygen the reaction can occur at lower residence times. With increasing oxygen content in the oxidizer the lowest residence time at blowout occurs closer to an equivalence ratio of 0.5. As shown in Figure 9, the lowest residence time for blowout occurs at an equivalence ratio of approximately 0.25 for pure oxygen, at 0.75 for air, and at roughly 1 for the 10% oxygen in the oxidizer mixture.

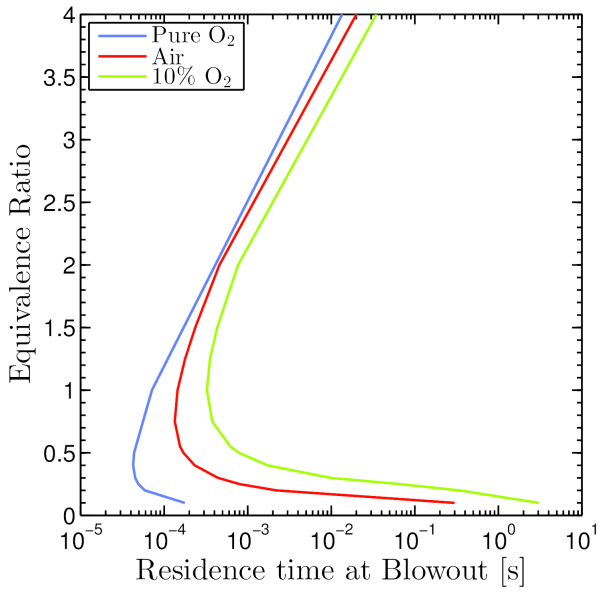

Figure 9: Residence times at blowout at various O_2 content in the oxidizer.

CHAPTER 4

LAMINAR DIFFUSION FLAMES

4.1 Introduction

This chapter deals with laminar diffusion flames established in an opposed-jet or counterflow configuration. This configuration has been extensively employed in numerous experimental and numerical studies. It is fundamental in combustion research because it approximates a one-dimensional flame and because the residence time can be easily modified. The counterflow flames provide important understanding of the detailed structure of diffusion flames and their extinction characteristics.

To explain the basic features of the counterflow flame, a typical experimental configuration is represented in Figure 10. Between the fuel and oxidizer jets lies the stagnation plane, where the axial velocity is zero ($v_x = 0$). Its location depends on the relative magnitudes of the oxidizer and fuel stream momentum fluxes. When the condition of equal momentum fluxes ($\dot{m}_F v_F = \dot{m}_O v_O$) is imposed, the stagnation plane is at the midpoint between the nozzles. If the momentum flux of one of the stream is increased compared to the other, the stagnation plane moves towards the low-momentum-flux stream nozzle.

Combustion occurs in a thin reacting layer close to the stagnation plane, precisely where the mixture fraction is stoichiometric. This position defines the location of the reaction zone.

An important characteristic of the opposed flow arrangement is that the flame is nearly one-dimensional [22].

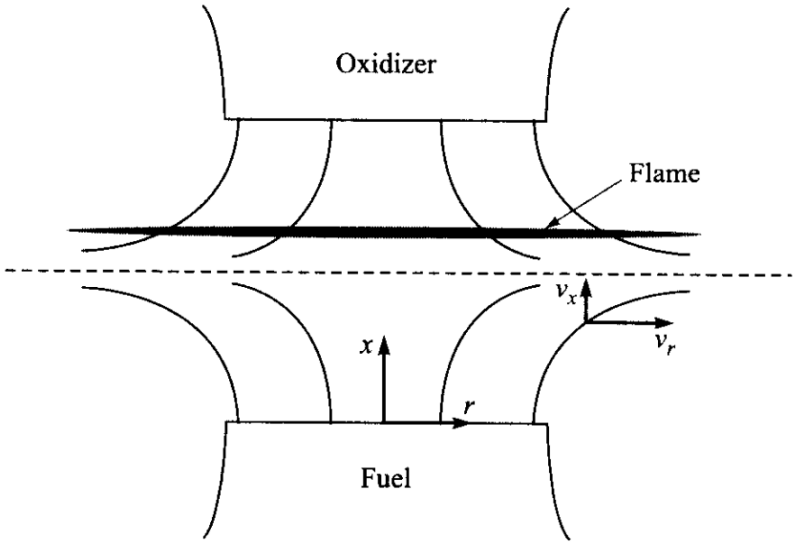

Figure 10: Counterflow flame arrangement.

4.2 CHEMKIN Governing Equations for Opposed-Flow Flames

The following section is extracted from CHEMKIN Manual [24].

This section describes the theoretical model including the conservation equations that govern the behavior of opposed-flow flames. A similarity transformation is employed to that reduce the 2-D system to a 1-D. This discussion pertains to the

CHEMKIN Reactor Models: Diffusion or Premixed Opposed-Flow Flame and Premixed Burner-Stabilized Stagnation Flame. [24]

4.3 Axisymmetric and Planar Diffusion

The following section is extracted from CHEMKIN Manual [24].

For the Opposed-Flow Flame model, a steady-state solution is computed for either axisymmetric or planar diffusion flames established between two opposing nozzles. The two or three-dimensional flow is reduced mathematically to one-dimension by assuming that the y- or radial velocity varies linearly in the y- or radial direction, which leads to a simplification in which the fluid properties are functions of the axial distance only. The one-dimensional model then predicts the species, temperature, and velocity profiles in the core flow between the nozzles. Both premixed and non-premixed flames can be simulated.

The axisymmetric geometry consists of two concentric, circular nozzles directed towards each other, as shown Figure 11(a). This configuration produces an axisymmetric flow field with a stagnation plane between the nozzles. The planar geometry consists of two concentric linear nozzles directed towards each other as shown in Figure 11(b). This configuration produces a 2-D planar flow field with a stagnation line between the two nozzles. The location of the stagnation plane depends on the momentum fluxes of the two streams. When the streams are premixed, two premixed flames exist, one on each side of the stagnation plane. When the two streams

contain fuel and oxidizer, respectively, a diffusion flame is established. Since most fuels require more air than that based on stoichiometry, the diffusion flame usually sits on the oxidizer side of the stagnation plane, i.e., the fuel diffuses through the stagnation plane to establish the flame corresponding to stoichiometric condition.

The Opposed-Flow Flame Simulator used in CHEMKIN is based on a model that was originally developed by Kee, et al. [27] for premixed opposed-flow flames. The reduction of the three-dimensional stagnation flow is based upon similarity solutions advanced for incompressible flows by von Karman [28], which can be found in Schlichting [29]. Moreover, CHEMKIN impinging and stagnation-flow models are based on a finite domain, where the user specifies the nozzle separation. For this approach, an eigenvalue must be included in the solution of the equations and the strain rate varies, such that a characteristic strain rate must be determined from the velocity profile. Following the analysis of Evans and Grief [30], Kee, et al. [27] showed that this formulation allowed more accurate predictions of the extinction limits for premixed flames than other approaches.

The geometry for the axisymmetric and planar configurations is sketched in Figure 11(a) and Figure 11(b), respectively. In the following equations, ξ represents either the radial direction r for the axisymmetric case, or the perpendicular direction y for the planar case. The coordinate parameter n allows us to present one set of equations for both cases, with $n = 3$ for the 3-D axisymmetric flow and $n = 2$ for

the 2-D planar case. A more detailed derivation of the governing equations for the opposed-flow geometry has been provided by Kee, et al. [27].

At steady-state, conservation of mass in cylindrical or planar coordinates is

$$\frac{\partial(\rho u)}{\partial x} + \frac{1}{\xi^{n-2}} \frac{\partial(\rho v_\xi \xi^{n-2})}{\partial \xi} = 0 \tag{4.1}$$

where u and v_ξ are the axial and radial (or cross-flow) velocity components, and ρ is the mass density.

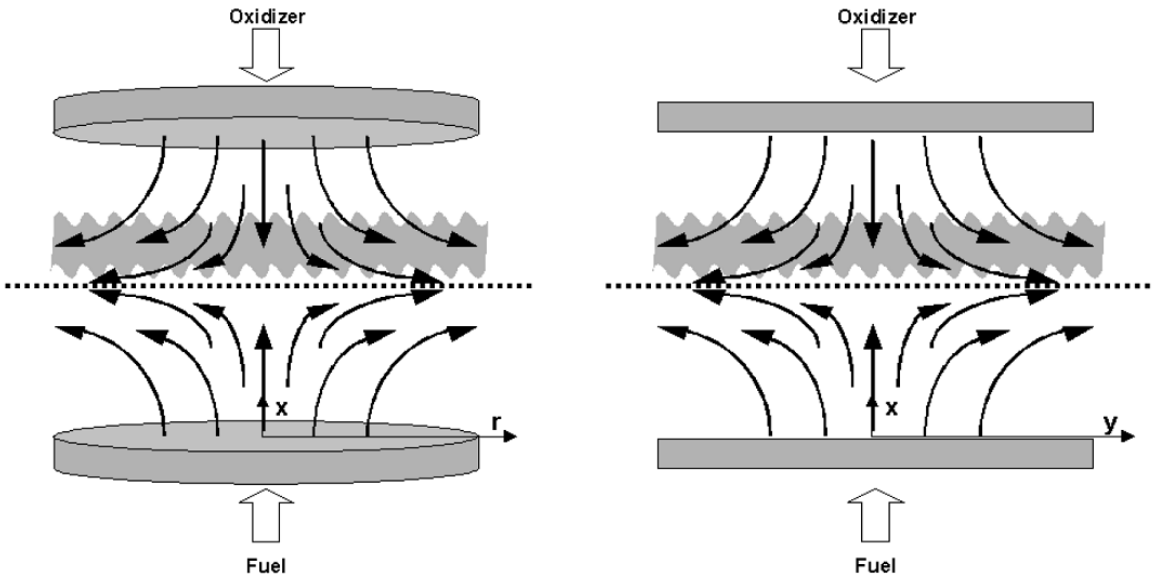

(a) (b)

Figure 11: Geometry of the axisymmetric and planar opposed-flow diffusion flame.

Following von Karman [28], who recognized that v_ξ and other variables should be functions of x only, we define

$$G(x) = \frac{-(\rho v_\xi)}{\xi} \qquad F(x) = \frac{\rho u}{(n-1)} \tag{4.2}$$

Then the continuity Equation 4.2 reduces to

$$G(x) = \frac{dF(x)}{dx} \tag{4.3}$$

for the axial velocity u . Since F and G are functions of x only, so are ρ, u, T and Y_k.

The perpendicular momentum equation is satisfied by the eigenvalue

$$H = \frac{1}{\xi^{n-2}} \frac{\partial p}{\partial \xi} = \text{constant} \tag{4.4}$$

The equation of the perpendicular momentum is

$$H - (n-1)\frac{d}{dx}\left(\frac{FG}{\rho}\right) + \frac{nG^2}{\rho} + \frac{d}{dx}\left[\mu \frac{d}{dx}\left(\frac{G}{\rho}\right)\right] = 0 \tag{4.5}$$

Energy and species conservation are

$$\rho u \frac{dT}{dx} - \frac{1}{c_p}\frac{d}{dx}\left(\lambda \frac{dT}{dx}\right) + \frac{\rho}{c_p}\sum_k c_{pk} Y_k V_k \frac{dT}{dx} + \frac{1}{c_p}\sum_k h_k \dot{\omega}_k + \frac{1}{c_p}\dot{Q}_{rad} = 0 \tag{4.6}$$

where $\dot{Q}_{rad}$ is the heat loss due to gas and particle radiation.

$$\rho u \frac{dY_k}{dx} + \frac{d}{dx}(\rho Y_k V_k) - \dot{\omega}_k W_k = 0 \qquad k = 1, ..., K \tag{4.7}$$

where the diffusion velocities are given by either the multicomponent formulation

$$V_k = \frac{1}{X_k \overline{W}} \sum_{j \neq k}^{K} W_j D_{k,j} \frac{dX_j}{dx} - \frac{dD_k^T}{\rho Y_k} \frac{1}{T} \frac{dT}{dx} \tag{4.8}$$

or the mixture-averaged formulation

$$V_k = -\frac{1}{X_k} D_{km} \frac{dX_k}{dx} - \frac{D_k^T}{\rho Y_k} \frac{1}{T} \frac{dT}{dx} \qquad \text{where} \qquad D_{km} = \frac{1 - Y_k}{\sum_{j \neq k}^{K} \frac{X_j}{\mathcal{D}_{jk}}} \tag{4.9}$$

and $D_{k,j}$, D_{km}, $\mathcal{D}_{jk}$ and D_k^T are the multicomponent, mixture-averaged, binary, and thermal diffusion coefficients, respectively.

The boundary conditions for the fuel (F) and oxidizer (O) streams at the nozzles are

$$x = 0: \qquad F + \frac{\rho_F u_F}{(n-1)}; \quad G = 0; \quad T = T_F; \quad \rho u Y_k + \rho Y_k V_k = (\rho u Y_k)_F \tag{4.10}$$

$$x = L: \qquad F + \frac{\rho_O u_O}{(n-1)}; \quad G = 0; \quad T = T_O; \quad \rho u Y_k + \rho Y_k V_k = (\rho u Y_k)_O \tag{4.11}$$

The inflow boundary condition (Equation 4.10 and Equation 4.11) specifies the total mass flux, including diffusion and convection, rather than the fixing species

mass fraction $Y_k = Y_{k,F}$. If gradients exist at the boundary, these conditions allow diffusion into the nozzle.

The differential Equation 4.3 through Equation 4.7 and boundary conditions (Equation 4.10 and Equation 4.11) form a boundary value problem for the dependent variables (F,G,H,T,Y_k). The GAS-PHASE KINETICS Subroutine Library provides the reaction rates and thermodynamic properties, while the TRANSPORT package evaluates the transport properties for these equations. [24]

4.4 Finite-difference Approximations

The following section is extracted from CHEMKIN Manual [24].

Discretization of the differential equations uses conventional finite differencing techniques for non-uniform mesh spacing. Diffusive terms use central differences, with truncation error that is second-order in the mesh spacing. For better convergence, convective terms use upwind differencing, which uses the sign of the velocity to choose which direction the spatial difference will go. If $u_j = 0$, for example, then the convective term in the energy equation is differenced as:

$$\rho u \frac{dT}{dx} \approx \rho_j u_j \left(\frac{T_j - T_{j-1}}{x_j - x_{j-1}} \right) \tag{4.12}$$

The truncation error of this approximation is first-order in the mesh spacing, leading to what is often called artificial diffusion, but this form avoids unwanted oscillations during the solution on a coarse mesh. [24]

4.5 Regrid Operation

The following section is extracted from CHEMKIN Manual [24].

A Regrid operation is specified by supplying a new number of grid points during a restart or continuation, which allow a new flame solution to begin from an initial guess based on the solution of a previous flame.

The steady-state solver, TWOPNT, automatically refines the grid by adding points in regions where they are needed to resolve the first and second derivatives of the solution, using criteria controlled by the Gradient and Curvature grid parameters. However, TWOPNT does not move or remove points. If it reaches a maximum number of points (internally defined by the dimensions), a warning message is printed and the adaptation is terminated. In some cases, then, it may be necessary to reduce the number of points when starting a new solution from a previous result. The Regrid operation redefines the solution guess on the user-specified number of mesh points.

The Regrid operation is different from the grid-point insertion operation performed by TWOPNT. Both operations attempt to resolve the gradient and curvature in the solution, except that TWOPNT considers all solution components, whereas Regrid only considers the temperature profile. TWOPNT only adds points, leaving the old points as they were, but Regrid alters the location and solution of all the points interior to the boundaries. Regrid computes new locations for exactly the

given number of points, and then interpolates the solution from the previous grid to obtain a new approximation of the solution. Regrid does not conserve any properties of the solution; in fact, it tends to smooth the solution by the error inherent in the interpolation.

Regrid redistributes a weighting function of the first and second derivatives of the temperature. The profiles of the other dependent variables are ignored on the assumption that the temperature profile defines the flame location well enough for the purposes of realigning the mesh for an initial condition. The redistribution uses a transformation from the physical coordinate x to a new coordinate η

$$\frac{dx}{d\eta}W(x,T) = C \tag{4.13}$$

with the weighing function,

$$W(x,T) = 1 + b_1\left|\frac{dT}{dx}\right| + b_2\left|\frac{d^2T}{dx^2}\right| \tag{4.14}$$

Integration over the entire domain defines the constant

$$C = \frac{1}{N-1}\int_0^L W(x,T)dx \tag{4.15}$$

Integrating over a portion of the domain gives an expression for the point locations in η-space

$$\eta = 1 + \frac{1}{C}\int_0^x W(x,T)dx \tag{4.16}$$

The new grid locations x come by interpolation between the computed values of η defined using the old mesh, onto a uniform mesh in η-space. Since $d\eta$ is constant on this uniform mesh, the solution to Equation 4.13 states that $W(x,T)dx$ is constant, so the new values of x will be concentrated where the weighting function is large.

Table V is a sample set of parameters that would direct the Opposed-Flow Flame Model to perform the Regrid operation during a restart. These parameters are specified in the Cluster Properties Panel, when Restart problem-type is chosen. This sequence will create a new solution guess on 20 points, devoting 60 percent of the points to resolving gradients, with equal weighting of gradient and curvature in the temperature profile. From experience, it is recommended to use a value greater than or equal to 1 for the gradient to curvature adaptation ratio. Depending on the resolution of the existing solution, the percent of grids used in the regrid process should be in the neighborhood of 50%. Using 0 percent grids for regrid results in a uniform mesh. [24]

TABLE V: REGRID PARAMETER EXAMPLES

Parameter	**Value**
Number of Grid Points for Regrid	20
Percent of Grids for Regrid	0.6
Ratio of Gradient to Curvature Adaptation	1.0

4.6 Set Up an Opposed-Flow Flame Calculation on CHEMKIN

Analogously to the chemical equilibrium calculation, the first step to correctly set up a simulation is the creation of a new project file. The user then selects in the models panel the type of reactor he is willing to use and drag its icon into the diagram view window. In this case, Diffusion or Premixed Opposed-Flow flame is chosen. This kind of configuration requires the connection of two external sources of inlet gas, one for the fuel and the other for the oxidizer, and one outlet flow. Again, CHEMKIN requires the definition of the chemical kinetic mechanism, employed for the simulation. Most of the calculations are carried out using the San Diego mechanism [16], which comes with three data files, the Gas-Phase Kinetics File, the Thermodynamics Data File, and the Gas Transport Data File. After preparing the chemistry set, one should define the physical parameters of the simulation. The type of problem solved in this matter is the Gas Energy Equation. The grid properties are to be specified as well, in particular the ending axial position, which represents the distance between fuel and oxidizer

nozzles. Then, the user should set the stream properties, that are the inlet velocity and the inlet temperature for both fuel and oxidizer sides, and the species-specific properties, including the mole fractions of the involved reactants. At this point, the simulation can be run. Once all the calculations are performed, CHEMKIN gives the possibility of exporting the outputs to an Excel sheet, allowing post-processing of the data.

4.7 Simulation Results

Simulations have been performed for diffusion flames in an opposed-jet configuration using the same two fuel mixtures as described earlier.

Different initial thermal conditions are simulated combined with the variation of the fraction of oxygen in the oxidizer. Eventually an extensive analysis of the extinction boundaries is provided.

To effectively compare the results for different initial conditions, it is essential to set up the important parameters. The distance between the two nozzles is taken as 2 cm and the pressure is 1 atm. Two different temperatures are considered for the fuel and air streams. Simulations are performed for different global strain rates and O2 mole fraction in the air stream. Note that the inverse of the strain rate defines a characteristic time for transport processes, and also provides the residence time for the chemical reactions to occur. The inlet velocities at the two nozzles are obtained from the following two equations:

$$a_s = \frac{2|V_O|}{L}\left(1 + \frac{|V_F|\sqrt{\rho_F}}{|V_O|\sqrt{\rho_O}}\right) \tag{4.17}$$

and to conform the conservation of momentum flux:

$$\rho_O V_O^2 = \rho_F V_F^2 \tag{4.18}$$

The first equation defines the global strain rate, while second one imposes the condition of equal momentum fluxes at the fuel and oxidizer nozzles. In these equations V and ρ are, respectively, the inlet velocity and density of fuel and oxidizer, and L is the distance between the nozzles.

Figure 12 presents the temperature and velocity profiles for the two cases investigated. As indicated in Figure 12(a), the peak temperature for the first case is 1519 K, and its location is 0.96 cm from the fuel nozzle The corresponding temperature for the second case is 1667 K, and its location is almost the same as that for the first case. The peak temperatures for the two flame cases are consistent with the corresponding equilibrium temperatures of 1593.8 K and 1767 K. The lower values for the flame cases are due to the transport processes and finite residence time imposed by the strain rate. The velocity profiles shown in Figure 12(b) locate the stagnation plane slightly upstream of the center plane, or closer to the fuel nozzle.

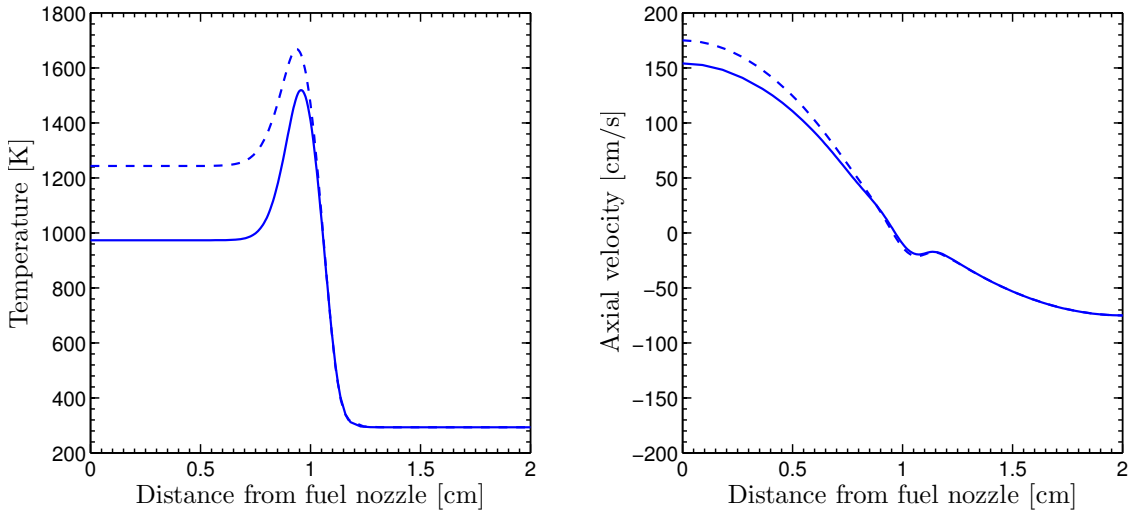

(a) (b)

Figure 12: Temperature and velocity profiles for counterflow diffusion flames. Solid and dashed lines correspond to Case 1 and Case 2. Strain Rate: 150 s^{-1}.

Figure 13 presents the species mole fraction profiles. To study the species profiles, they have been organized in three groups: major and minor species and NO_X compounds. Looking at Figure 13(a), the major species are reported. It is interesting to observe the local maxima reached by the main products of combustion, H_2O and CO_2. They are the results of the occurrence of the combustion process, during which H_2 and CO are burned. Focusing on the reactants, H_2 and CO, we can observe that they are both consumed during the combustion process. The respective mole fractions fall to near-zero values at the axial location where the

maximum temperature occurs. Always in Figure 13(b), the OH mole fraction profile is plotted and is regarded as a very important parameter to discern the location of the flame. In fact, together with the peak temperature, the location of the maximum production of OH is used to define the position of the flame. Figure 13(c) presents the NO and NO_2 profiles in the two flames. The amount of NO formed is significantly higher for case 2 compared to that for case 1. This is due to the higher peak temperature for flame 2 compared to that flame 1. As noted earlier the peak temperature for flame 2 is about 150 K higher that flame for flame 1. The NO_2 values are also higher for flame 2, although it mole fraction is considerably lower than that of NO.

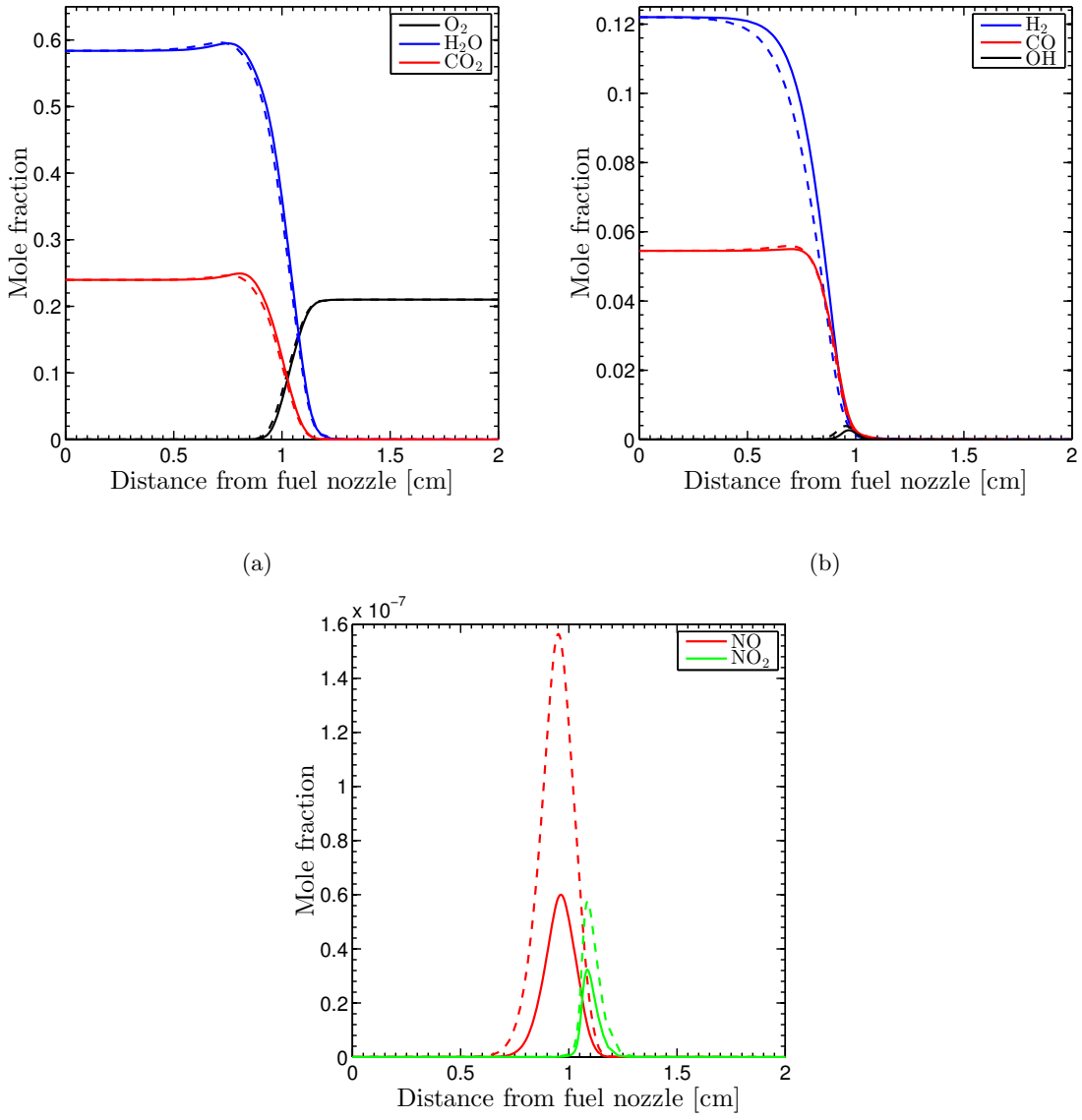

Figure 13: Major species (O_2, H_2O, CO_2), minor species (H_2, CO, OH) and NO_X mole fraction profiles for the two flames as discussed in Figure 12.

A global comparison for the two flames is presented in Table VI in terms of the peak heat release rate and total heat release rate. Both the peak and the integrated heat release rates are higher for flame 1 than for flame 2.

TABLE VI: INTEGRATED HEAT RELEASE RATE IN THE TWO CASES

Case #	**Peak Heat Release Rate** $[J/cm^3 \cdot s]$	**Integrated Heat Release Rate** $[J/cm^2 \cdot s]$
1	171.3	17.00
2	147.8	16.78

It is possible to conclude that even though the initial temperature of the fuel is increased, no relevant advantages are obtained, as far as counterflow flame combustion is considered. On the contrary, in the second case the peak and the integrated heat release rate are lower that the configuration at lower temperature. Moreover, the higher flame temperature reached in the second condition causes negative effects in terms of emission. The production of NO_X is greater than the first set up. For these reasons, one can assert that an increase in initial temperature of the fuel is not suitable when non-premixed counterflow flames are employed as mean of combustion.

4.8 Extinction Behavior of Counterflow Flames

In this section a detailed study on the extinction and NO_X characteristics of counterflow diffusion flames is reported. The extinction process is examined by varying the oxidizer composition, and extinction limits are presented in terms of the minimum O_2 mole fraction at extinction at different strain rates [31]. The study is motivated from two considerations. One is that the low-energy syngas mixture from the SOFC exhaust has high CO_2 and H_2O concentrations. Consequently, flames burning such fuels are prone to oscillations and extinction. Another motivation is to characterize the combustion and emission behavior of syngas mixtures from the SOFC exhaust stream.

Describing the combustion characteristics of a fuel, the study of the extinction behavior becomes very important for both scientific interest and more important from the safety considerations related to the flammability limits of the fuel. In addition, the investigation of the flame extinction conditions leads to a better understanding of which environmental and working configurations are the most convenient to employ such fuel.

The temperatures of fuel and oxidizer streams are assumed to be 700°C and 20°C, respectively. At the given strain rate of 150 s^{-1}, a diffusion flame is simulated using pure oxygen as oxidizer. Then, the O_2 fraction is reduced until flame extinction occurs.

Simulations using three detailed reactions mechanisms, namely the Davis [18], AramcoMech 1.3 [19], San Diego [16] are compared. Based on this comparison, the San Diego mechanism is employed for the detailed extinction study.

Figure 14 presents the extinction behavior in terms of the peak flame temperature versus O2 mole fraction, as predicted by the three mechanisms. There is good agreement between the peak temperatures predicted with the three mechanisms. Note that the peak temperature decreases from 1801 K to 1247.3 K as O_2 mole fraction is reduced from 100% to 10% for the San Diego mechanism. The minimum O_2 mole fractions at extinction for the three mechanisms are also fairly close, with the values being 10%, 9%, and 8% for the San Diego, Davis, and AramcoMech mechanisms, respectively. There are, however, some differences between the peak heat release rates, while the integrated heat release rate values are quite close [32], for the three mechanisms, as shown in Figures 14(b) and 14(c).

Moreover, it is interesting to note that for O_2 mole fraction less than 40%, the peak temperature becomes significantly more sensitive to the decrease in O_2 mole fraction, showing a sharper trend.

This behavior is related to the increase in the amount of unburned fuel for lower O_2 mole fractions, as indicated in Figure 15 which plots the H_2 and CO profiles for three different cases. In fact looking at Figure 15 we see that when the amount of available O_2 is low, the fuel does not completely transform into its products. This fact can be approximately visualized thanks to the vertical lines in Figures 15(a) and 15(b) representing the position of the flame. The length of the segment between the intersection of the curves and the horizontal axis is proportional to the amount of retained untransformed fuel. We notice that in the case corresponding to 10% of oxygen, the fraction of unburned H_2 and CO is significantly higher than those ones at higher percentage of oxygen.

The computed results can be used to determine the thermal efficiency associated with the diffusion flames. In order to examine the advantage of oxy-combustion, two cases are considered, one with air and the other with pure O2 in the oxidizer stream. The rate of energy flowing into the system is taken as the product of fuel mass flow rate and its lower heating value (LHV), see Equation 4.19 below, while the rate of energy produced through combustion is obtained by integrating the rate of heat release profile. The rate of energy flowing into the system is

$$\dot{Q}_{max} = \rho_F \cdot v_{x,F} \cdot LHV = 86.93 \frac{J}{cm^2 \cdot s} \tag{4.19}$$

As mentioned earlier, LHV is 1972.55 kJ/kg. Using the integrated heat release rate values, the thermal efficiency values for the air and pure oxygen cases are 0.195 in air and 0.316 respectively. Thus the thermal efficiency can be considerably enhanced using oxy-combustion.

Figure 14(d) presents temperature profiles for four different cases with 100%, 60%, 20% and 10% of O_2 in the oxidizer stream. As O_2 mole fraction decreases, the peak temperature decreases and the flame moves closer to the oxidizer nozzle.

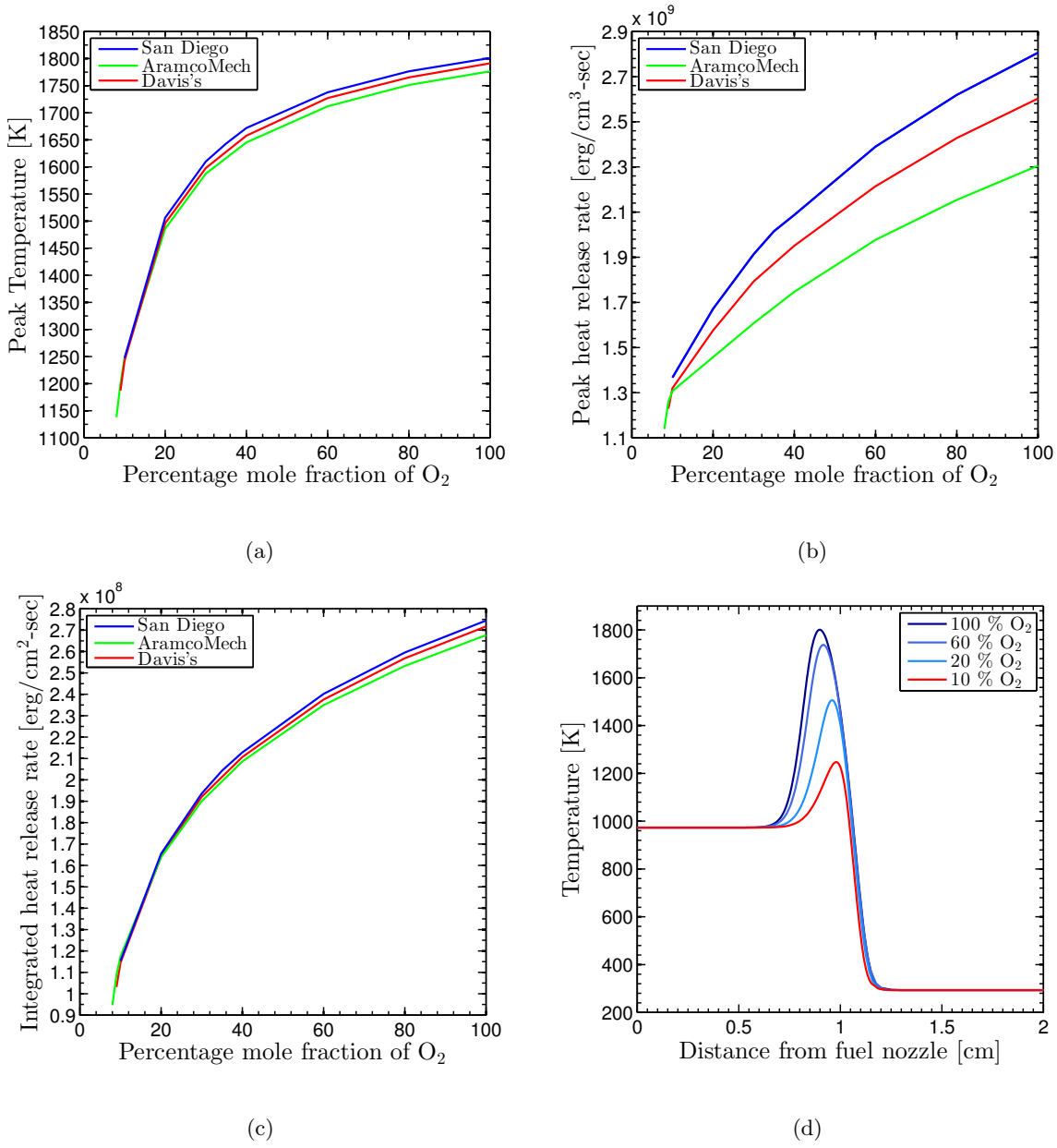

Figure 14: Peak temperature, peak heat release rate and integrated heat release rate plotted versus O_2 mole fraction in the oxidizer stream. Strain rate: 150 s^{-1}.

Figure 15 presents H_2, CO, CO_2, and OH profiles for different O_2 mole fractions in the oxidizer stream. The profiles indicate a typical diffusion flame structure, which is qualitatively the same for all the three cases. Fuel species (H_2 and CO) are consumed in the reaction zone, producing CO_2 and H_2O as the main product species. As indicated earlier, the flame shifts toward the oxidizer nozzle as the O_2 mole fraction in the oxidizer stream is decreased. This is indicated more clearly by the OH profiles. In addition, the OH peak value decreases as the O_2 mole fraction is reduced, indicating reduced reactivity. It is also interesting to mention that the CO mole fraction increases upstream of the flame, showing a local peak. This is due to the high diffusivity and reactivity of hydrogen, causing the H_2 mole fraction to decrease at a faster rate than that of CO.

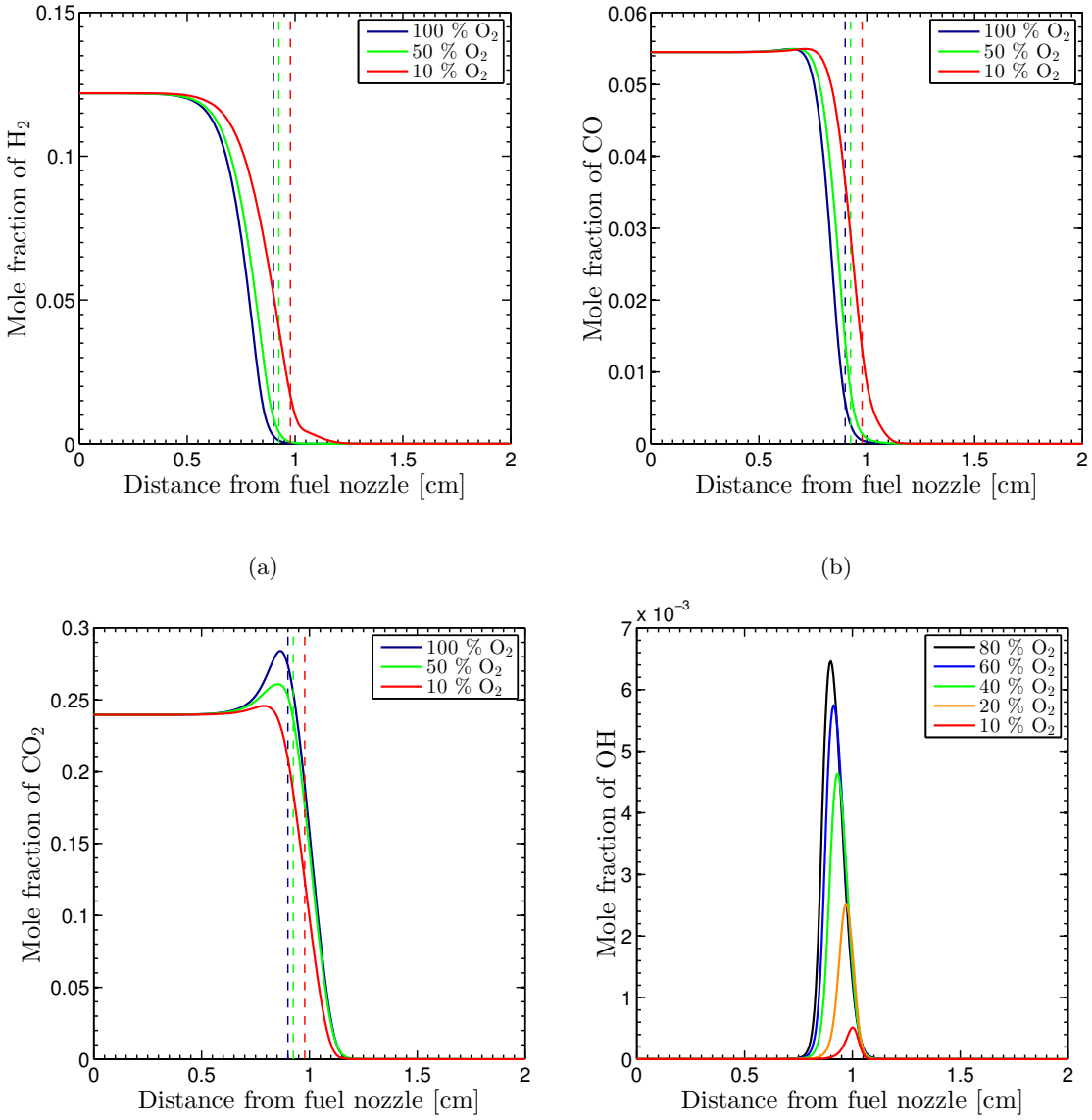

Figure 15: H_2, CO, CO_2 and OH mole fraction profiles for different O_2 mole fraction in the oxidizer stream.

Figure 16 presents the NO and NO_2 profiles for different O_2 mole fractions. As expected, these species are produced in the high temperature zone. An important observation is the existence of an optimum O_2 mole fraction corresponding to a minimum in NO formation. As O_2 fraction in the oxidizer stream is increased, the amount of NO formed first increases due to higher flame temperature (Figure 14). However, for O_2 fraction higher than 40%, the NO concentration decreases as O_2 fraction in the oxidizer stream is increased further. This is due to the effect of reduced N_2 concentration resulting in lower thermal NO formed. This further highlights the advantage of oxy-combustion in terms of higher flame temperature but lower NO_X emission. A similar behavior is observed with respect to the effect of O_2 on the NO_2 formation, except that NO_2 mole fraction is much smaller than that of NO, and the optimum O_2 fraction is between 20-40%.

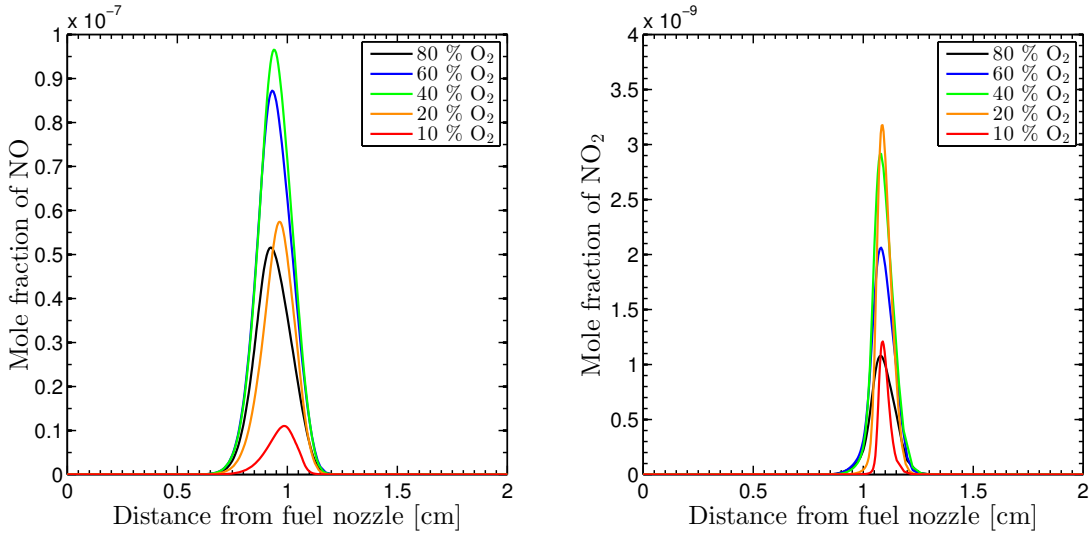

(a) (b)

Figure 16: NO and NO_2 profiles for different O_2 mole fraction in the oxidizer stream.

4.9 Flame Extinction Limits

Extinction limits are determined in terms of the extinction strain rate, representing flame blow out, for a given mole fraction of O_2 in the oxidizer stream. Results are presented in Figure 17 and Table VII. The strain rates and/or O_2 mole fractions below the curve (Figure 17) represent conditions for which a steady diffusion flame cannot be established for the given syngas mixture. For this mixture, the extinction strain rates range from 50 s^{-1} up to 2300 s^{-1} depending upon the O_2 fraction in the oxidizer stream. Thus for 100% O_2 in the oxidizer, a steady diffusion flame cannot be sustained at stain rates exceeding 2300 s^{-1}. Similarly, at a strain rate of 50 s^{-1}, the lowest O2 mole fraction for which a diffusion flame can be established is 8%. This limiting O2 fraction is referred as the limiting oxygen index (LOI) or critical oxygen limit [33]. It is also interesting to note that for the given syngas mixture with air as the oxidizer, a diffusion flame can be established for strain rates between 50 s^{-1} to 1400 s^{-1}.

TABLE VII: STRAIN RATES WITH CORRESPONDING MINIMUM PERCENTAGE MOLE FRACTION OF O_2 IN THE OXIDIZERS

Strain Rate [s^{-1}]	50	150	500	750	1000	1400	1500	1750	2000	2100	2300
Minimum O_2 %	8	10	13	15	17	21	23	28	34	36	43

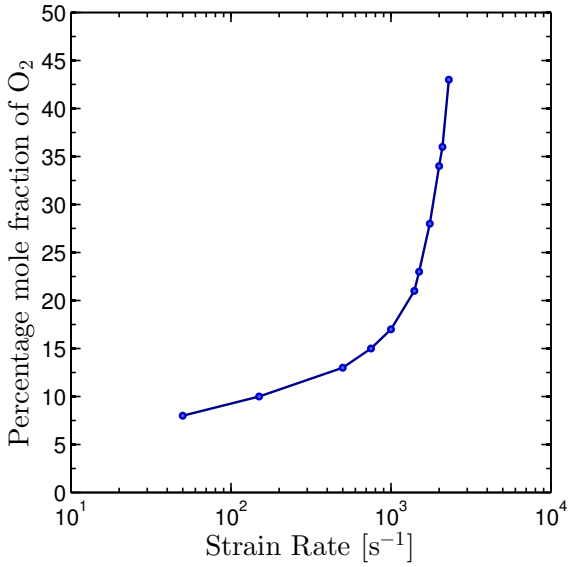

Figure 17: Extinction limits for syngas diffusion flames in terms of strain rate and O_2 mole fraction in the oxidizer.

CHAPTER 5

2-D LAMINAR FLAME SIMULATIONS

In this chapter, two-dimensional simulations are carried out to examine the detailed structure and extinction of counterflow non-premixed flames. The objective is to assess the validity of 1-D results, especially at extinction conditions, and to provide further insight into the extinction process. A previous study indicated that compared to the one-dimensional model, 2-D simulations provide better results for flames at limit conditions [5]. Detailed transport and chemistry models are incorporated into a CFD code, known as UNICORN [7] [8]. The same syngas mixture as that used for 1-D simulations, is considered. In the first part of this chapter, results focus on the diffusion flame structure and the comparison of 1-D and 2-D simulations. In the second part, the extinction behavior of diffusion flames is investigated.

5.1 Computational Model

The UNICORN (UNsteady Ignition and COmbustion using ReactioNs) is a two-dimensional, axisymmetric, time-dependent CFD code. It performs DNSs (direct numerical simulations) and has improved through an extensive experimental activity aimed to investigate its ability to predict ignition, extinction and stability limits of various flame configurations. Consequently, it has been extensively validated in previous studies using experimental data for a variety of flames and combustion phenomena in different configurations [5].

Based on a non-uniform grid system, the algorithm employs two momentum equations, enthalpy, species conservation and continuity equations to simulate the physical problem. Detailed thermo-transport and chemistry models are incorporated into the code. The fuel chemistry is modeled using the San Diego mechanism [16] containing 52 species and 544 reactions, as described earlier. A simple radiation model is also included within the code [34]. Further details about the functioning of the code are given in [8], [35], [36] and [37].

Figure 18 illustrates the computational domain for simulating counterflow diffusion flames. Similar to 1-D simulations, the flame is established using two opposing jets from two coaxial nozzles with syngas mixture flowing from one nozzle and oxidizer from the other. Due to the axisymmetric geometry, only one-half of the domain is considered in simulations. As discussed earlier, inlet velocities of the fuel and oxidizer jets are determined by specifying the global strain rate and enforcing the momentums of the two jets to be equal. The radii of the two nozzles are both equal to 14 mm, and the distance between them is 20 mm. An annular nitrogen coflow surrounds both the fuel and oxidizer jets. The computational domain is 20 mm in axial direction and 30 mm in radial direction. Simulations are performed using a 301 x 31 variable grid system. Boundary conditions include a symmetry condition at the left boundary, inflow conditions at the bottom and top boundaries and an outflow condition at the right boundary. At the two inflow boundaries, velocities, temperatures and species mass fractions are specified.

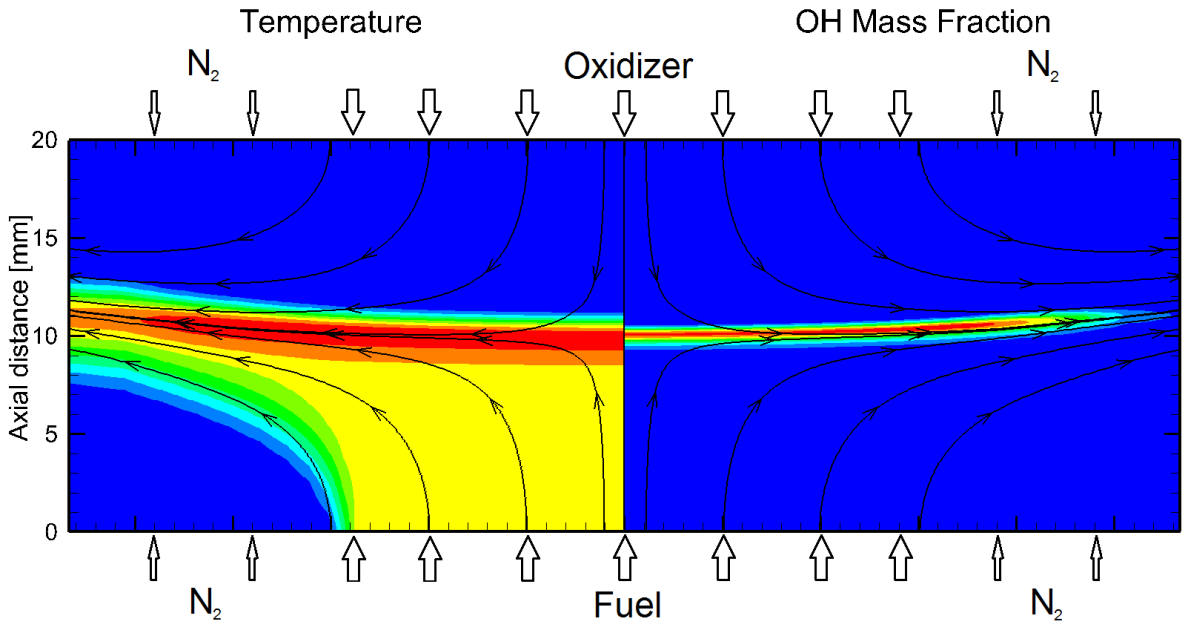

Figure 18: Physical and computational domain for simulating counterflow flames. Strain rate: 150 s^{-1}, O_2: 10%.

5.2 Numerical Procedure for Flame Calculation using UNICORN

UNICORN software contains two Fortran codes: unicorng2.f and unicornd-hept-sd.f. The first program employs a global one-reaction mechanism ($Fuel+O_2+N_2 = CO_2+H_2O+N_2$) and provides the initial conditions, in terms of velocity, species and temperature distribution, which are used by the second program containing the detailed mechanism. The input parameters are specified in an input file (input.uni), which is read by the executable to initiate the simulation.

The input file contains the geometry parameters (i.e., nozzle radii, distance between them, etc.), boundary conditions, the mesh system, and parameters for convergence of the computations.

The output from the Fortran is stored in a file (FLAMEA.DATA), which contains velocity, temperature, and species distribution in the flow field. A post processing Fortran code (unicorn-xyplots.f) is then used to plot and analyze the results. This code can produce 2-D results in terms of velocity vectors and iso-contours in a Tecplot [38] file, as well as 1-D data in terms of the axial and radial profiles of velocity, temperature, and species mass fractions.

5.3 Results and Discussion

Figure 19 depicts the computed structure in terms of axial temperature, velocity, and reactant species profiles for a moderately stretched diffusion flame (strain rate = 150 s^{-1}).

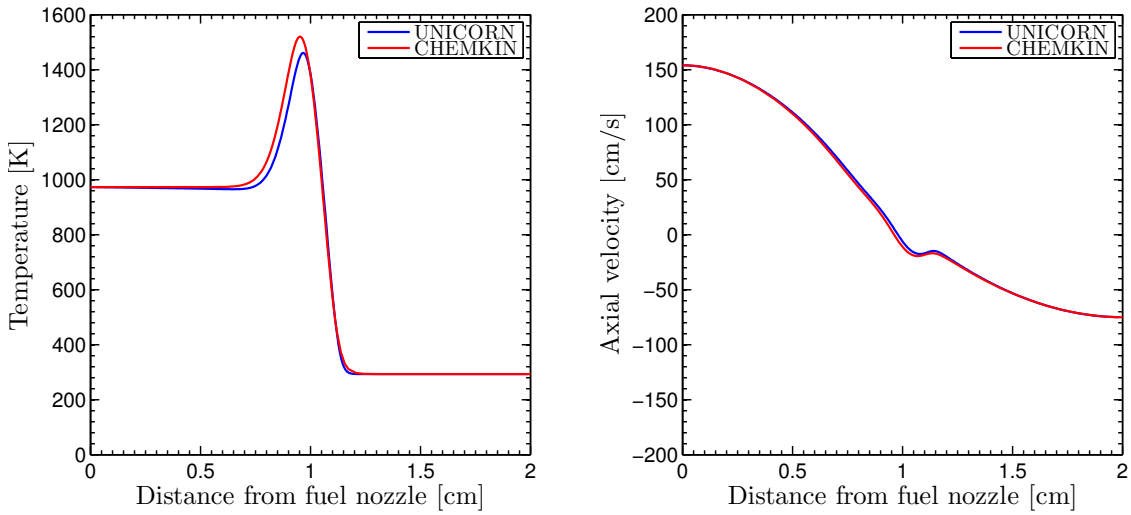

(a) (b)

Figure 19: Temperature and velocity profiles for syngas diffusion flames from 1-D and 2-D simulations.

The corresponding profiles of major product and radical species are shown in Figure 20 and Figure 21. Results are presented for both 1-D and 2-D simulations. Similar to the 1-D case, the fuel and air stream temperatures are 973.15 K and 293.15 K, respectively. All the other geometric and flow parameters are the same for 1-D and 2-D simulations. Overall there is good agreement between the 1-D and 2-D predictions, establishing the viability of 1-D approach for flames that are far from extinction. Radical species profiles indicate some differences, with the peak mole fractions of O, H, and OH being somewhat lower for the 2-D case, indicating slightly lower flame reactivity for this case. The lower reactivity for the 2-D case is also indicated by the temperature and major reactant (H_2 and CO) and product (CO_2 and H_2O) species profiles.

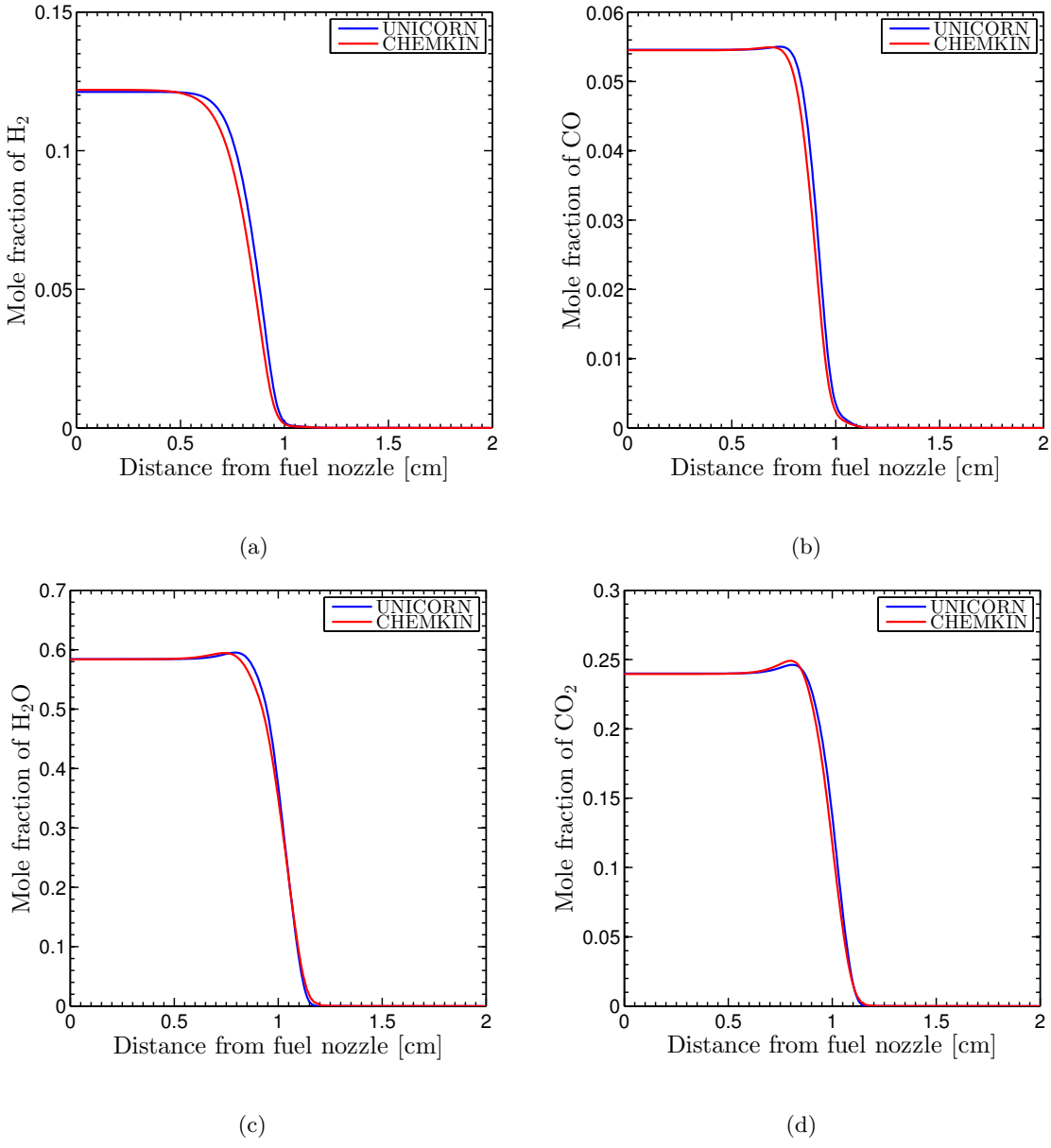

Figure 20: Major species profiles for syngas diffusion flames from 1-D and 2-D simulations.

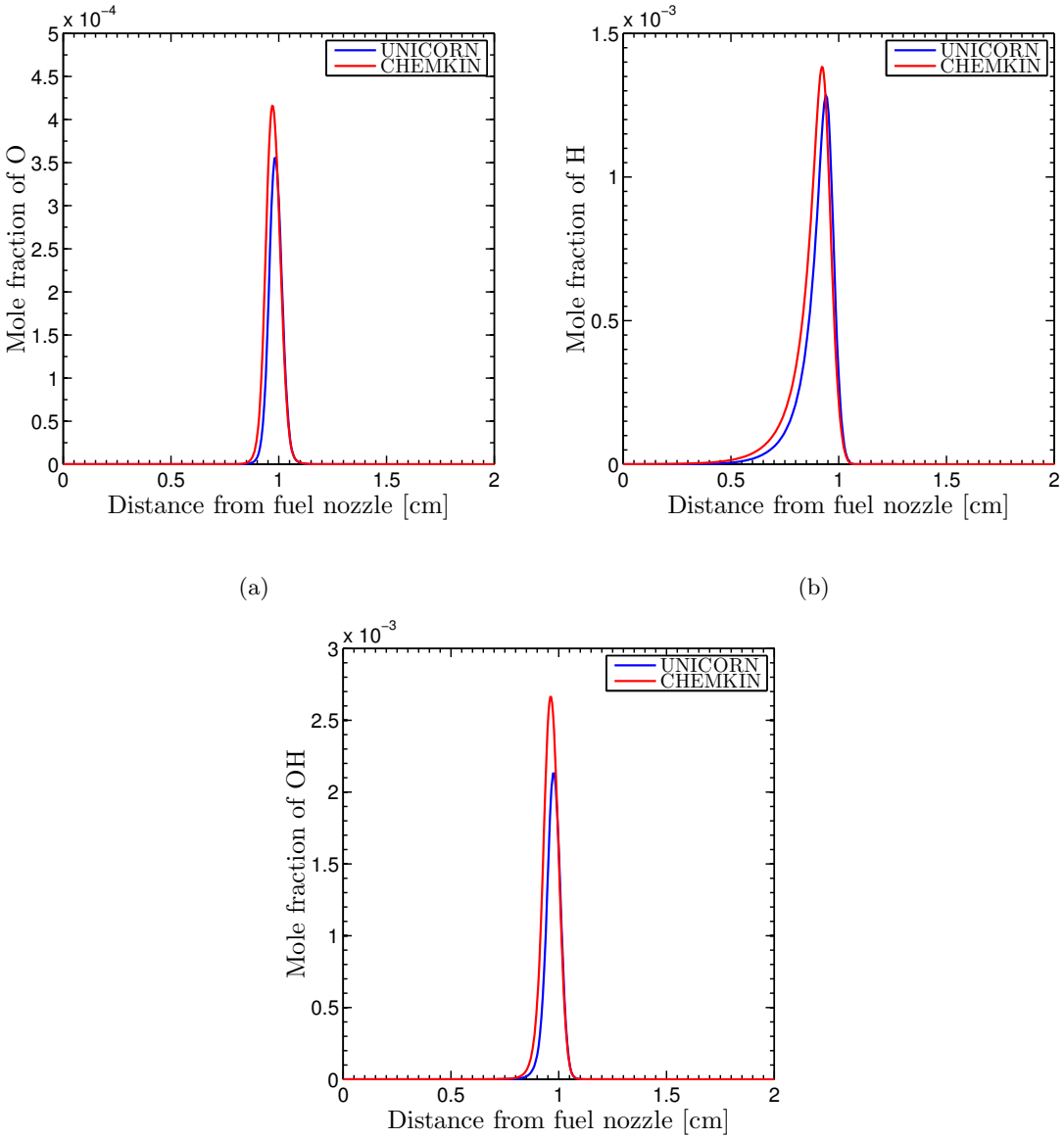

Figure 21: Radical species profiles for syngas diffusion flames from 1-D and 2-D simulations.

Similar to the 1-D case, the dilution-induced flame extinction is examined by lowering O_2 mole fraction (X_{O_2}) in the oxidizer stream. Figure 22 plots the peak flame temperature as a function of O2 mole fraction for both 1-D and 2-D simulations. The strain rate is 150 s^{-1}. As expected, the peak temperature decreases monotonically with the decreases in X_{O_2}, and flame is extinguished at $X_{O_2} \approx 0.1$. In addition, results indicate good agreement between the 1-D and 2-D predictions of flame extinction, except for a slightly lower temperature for the latter case, which is consistent with the 1-D and 2-D temperature profiles discussed earlier.

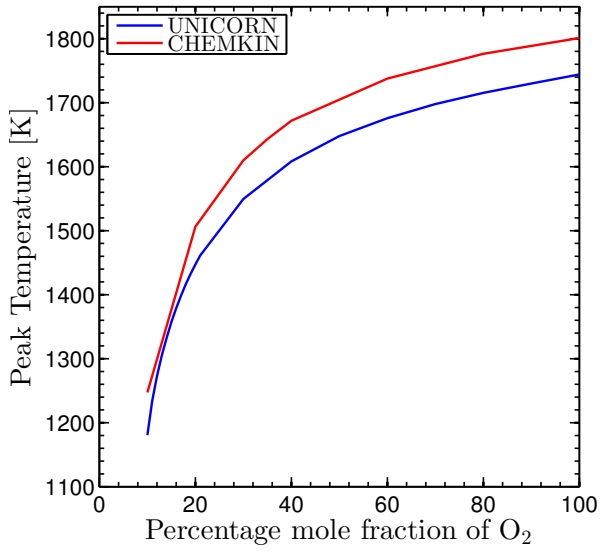

Figure 22: Peak flame temperature plotted versus O_2 mole fraction in the oxidizer stream, indicating dilution-induced extinction for both 1-D and 2-D simulations. Strain Rate: 150 s^{-1}.

The 2-D computational model can provide further insight regarding the flame structure and extinction behavior. This is illustrated in Figure 23, which presents the temperature and OH mole fraction contours for four different O_2 mole fractions. As X_{O_2} is reduced, the flame reactivity decreases as indicated by lower temperatures and reduced radical (OH) pool. Further discussion on this aspect in terms of scalar dissipation rate is provided in the next section.

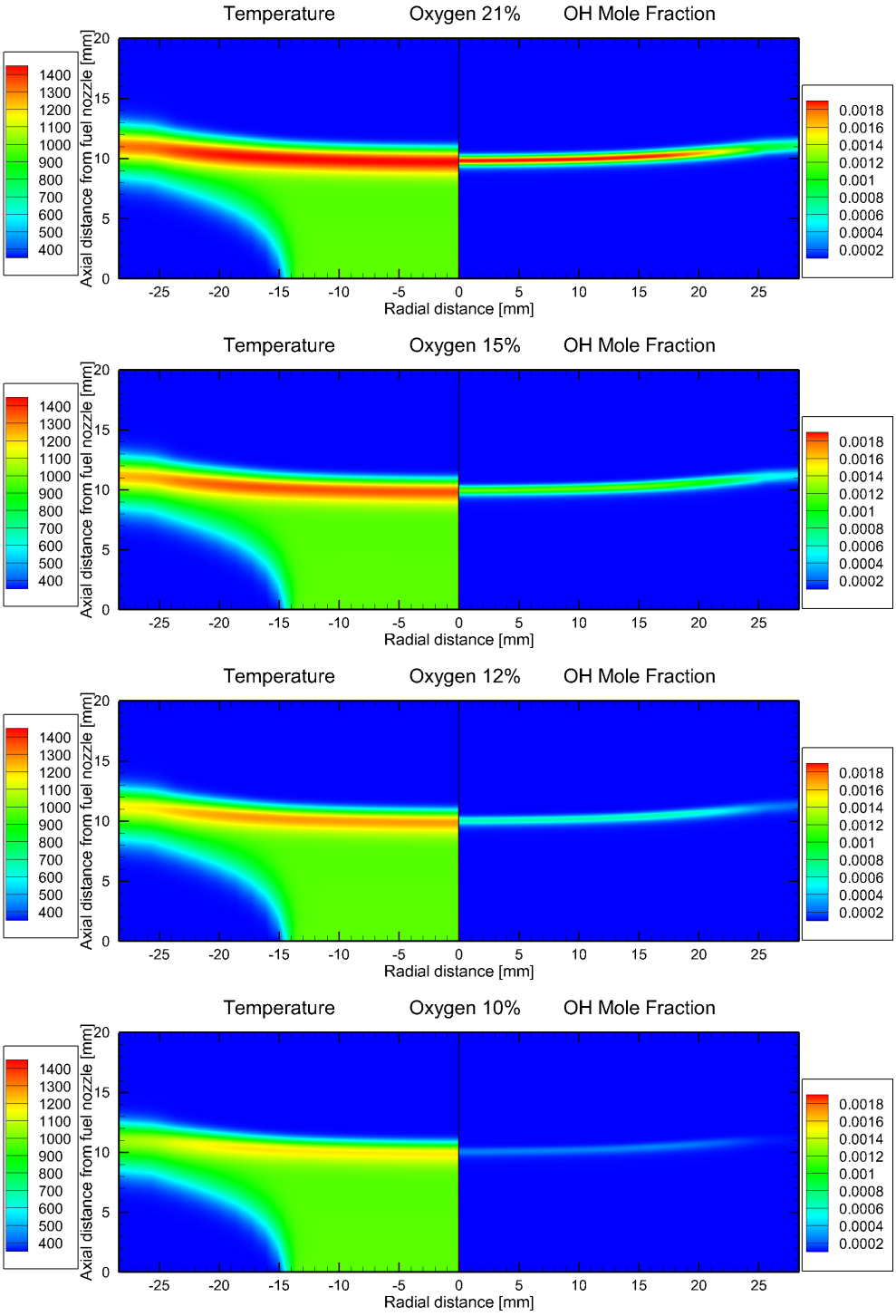

Figure 23: Temperature [K] and OH mole fraction contours for flames established with different O_2 mole fractions in the oxidizer stream. For 10% O_2 case, the flame is near extinction. Strain Rate:150 s^{-1}.

CHAPTER 6

SYNGAS FLAME EXTINCTION

USING MULTIDIMENSIONAL CFD CODE

In the present chapter we extend the study performed in the previous sections to a syngas mixture with 50% H_2 and 50% CO. The inlet temperatures of fuel and oxidizer streams are both equal to 300 K. Simulations are performed using both the 1-D CHEMKIN the 2-D CFD UNICORN codes. The focus is on the effect of strain rate and O_2 mole fraction on the flame extinction behavior. The opposed flow configuration is essentially the same as that used in the previous section, except that the distance between the two nozzles is 15 mm. The radii of fuel and oxidizer nozzles are equal to 14 mm. The computational domain is 15 mm and 30 mm in the axial and radial directions, respectively, with a 301 x 31 variable grid system. The methodology for specifying boundary conditions is the same as discussed earlier. Figure 24 provides an illustration of the computed 2-D flame structure in terms of temperature and OH mole fraction contours.

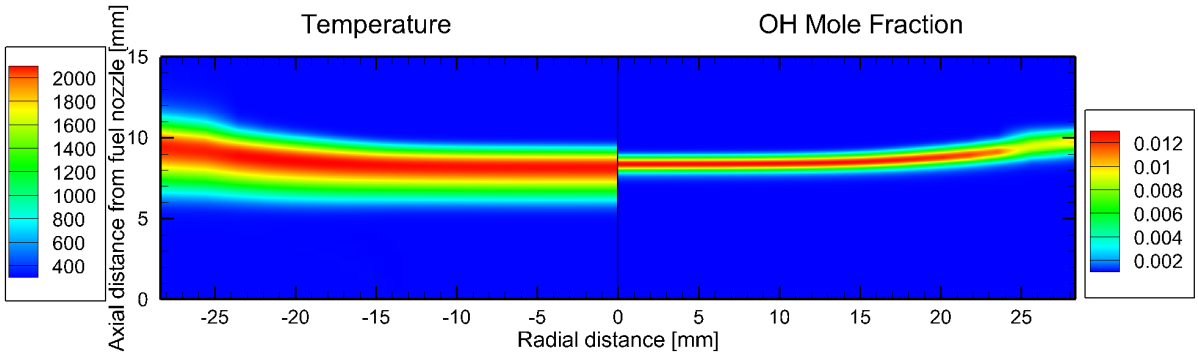

Figure 24: Example of steady state counterflow flame. Temperature [K] and OH mole fraction contours are represented.

6.1 Extinction Behavior of Counterflow Diffusion Flame

The extinction of a flame can occur due to several factors, such as an excessively high strain rate or a too low oxygen concentration in the oxidizer stream. To obtain a deeper understanding of the extinction phenomena, results are presented for dilution-induced extinction, and extinction conditions are extensively studied. The scalar dissipation rate has been employed as a useful analytical tool to characterize the extinction behavior of a flame. For instance, the strain rate is increased for an opposed-flow diffusion flame, the fuel and oxidizer concentration gradients in the mixing layer also increase. This decreases the local diffusion time and thus the Damköhler number (Da) in the flame vicinity, leading to stretch-induced extinction of the flame [39]. The scalar dissipation rate is defined as [3]:

$$\chi = 2D\left(\frac{\partial \xi}{\partial x_\alpha}\right)^2 = 2D_{F-mix}\left[\left(\frac{\partial \xi}{\partial x}\right)^2 + \left(\frac{\partial \xi}{\partial y}\right)^2 + \left(\frac{\partial \xi}{\partial z}\right)^2\right] \tag{6.1}$$

where D_{F-mix} is the fuel diffusivity with respect to the mixture and ξ is the mixture fraction, defined as the mass fraction of material originating in the fuel stream. The mixture fraction may be defined as:

$$\xi = \frac{Z_F - Z_{F,l}}{Z_{F,r} - Z_{F,l}} \tag{6.2}$$

The subscript F stands for one or a combination of elements, such as C and H, in the fuel stream, and subscripts l and r refer to the fuel-lean and fuel-rich streams, respectively. Z is defined as:

$$Z = \sum_{i=1}^{N_C} n_{C,i} \cdot Y_{C,i} \frac{M_C}{M_{C,i}} + \sum_{i=1}^{N_H} n_{H,i} \cdot Y_{H,i} \frac{M_H}{M_{H,i}} \tag{6.3}$$

Here N_C and N_H are the number of species containing carbon and hydrogen, respectively, $n_{C,i}$ and $n_{H,i}$ are the number of carbon or hydrogen in the ith species, $Y_{C,i}$ and $Y_{H,i}$ are the mass fraction of the ith species containing carbon or hydrogen, M_C and M_H are the molecular weights of carbon and hydrogen, respectively, $M_{C,i}$ and $M_{H,i}$ are the molecular weights of the ith species containing carbon or hydrogen.

The molecular diffusivity is computed using

$$D_{i-j} = \left[0.2669 \times 10^{-6} \frac{T^{3/2}}{P \cdot \sigma_{ij}^2 \sqrt{MW_i}\Omega_D(T^*)}\right] \tag{6.4}$$

The Lennard-Jones average collision diameters σ_i and the collision integrals $\Omega_D(T^*)$ are employed to compute the binary diffusion coefficient between each species and nitrogen (D_{i-N_2}). The fuel diffusivity is then calculated using the following equation:

$$D_{i-mix} = \frac{1 - X_i}{\sum_{\substack{j=1 \\ j \neq i}}^{N} (X_j / D_{ij})} \tag{6.5}$$

Where X_i is the mole fraction of the ith species.

Also note that the mixture fraction is uniquely related to the equivalence ratio through:

$$\xi = \frac{\phi}{(A/F)_{st} + \phi} \tag{6.6}$$

Corresponding to an equivalence ratio $\phi = 1$, the stoichiometric mixture fraction can then be calculated using

$$\xi_s = \frac{1}{(A/F)_{st} + 1} \tag{6.7}$$

The stoichiometric mixture fraction is useful while discussing the state relationships. The computation of the mixture fraction and the scalar dissipation rate for 2-D flame simulations was implemented in the post-processing Fortran code. Since UNICORN is a time dependent code, it allows one to examine the temporal evolution of the flame undergoing extinction. In the following, results are presented for both the stretched-induced and dilution-induced extinction of diffusion flames. For these results, the fuel stream consists of 50% H_2 and 50% CO, whereas

the oxidizer stream is air (21% O_2, 79% N_2). The strain rate for the base case is taken as 150 s^{-1}.

6.2 Stretch-Induced Extinction

The stretched-induced extinction is examined by performing 1-D and 2-D simulations at increasingly higher strain rates [40]. Figure 25 shows the extinction process in terms of the peak temperature as a function of global strain rate for both 1-D and 2-D cases. As the strain rate is increased, the peak temperature decreases due to a shortcoming of produced heat with respect to heat transported away from the flame [5]. There is fairly good agreement between the 1-D and 2-D predictions. Similar the results discussed earlier, the peak temperature is slightly lower for the 2-D case, with the maximum difference being 45 K corresponding to the strain rate of 150 s^{-1}. The extinction strain rated obtained from the 1-D and 2-D simulations are 525 s^{-1} and 515 s^{-1}, respectively. The corresponding peak temperatures at extinction are 2064 K and 2048 K, respectively.

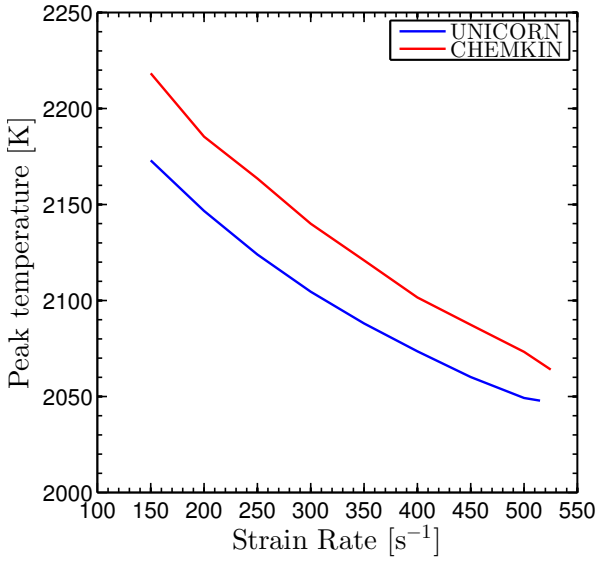

Figure 25: Variation of peak flame temperature with strain rate, indicating stretch-induced extinction for both 1-D and 2-D simulations.

Figure 26 depicts the detailed flame structure in terms of temperature and OH mole fraction contours for four different strain rates. As the strain rate is increased, the flame extinction process is indicated by the decrease in OH and temperature peaks, and by narrowing of OH contours or thinning of the reaction zone.

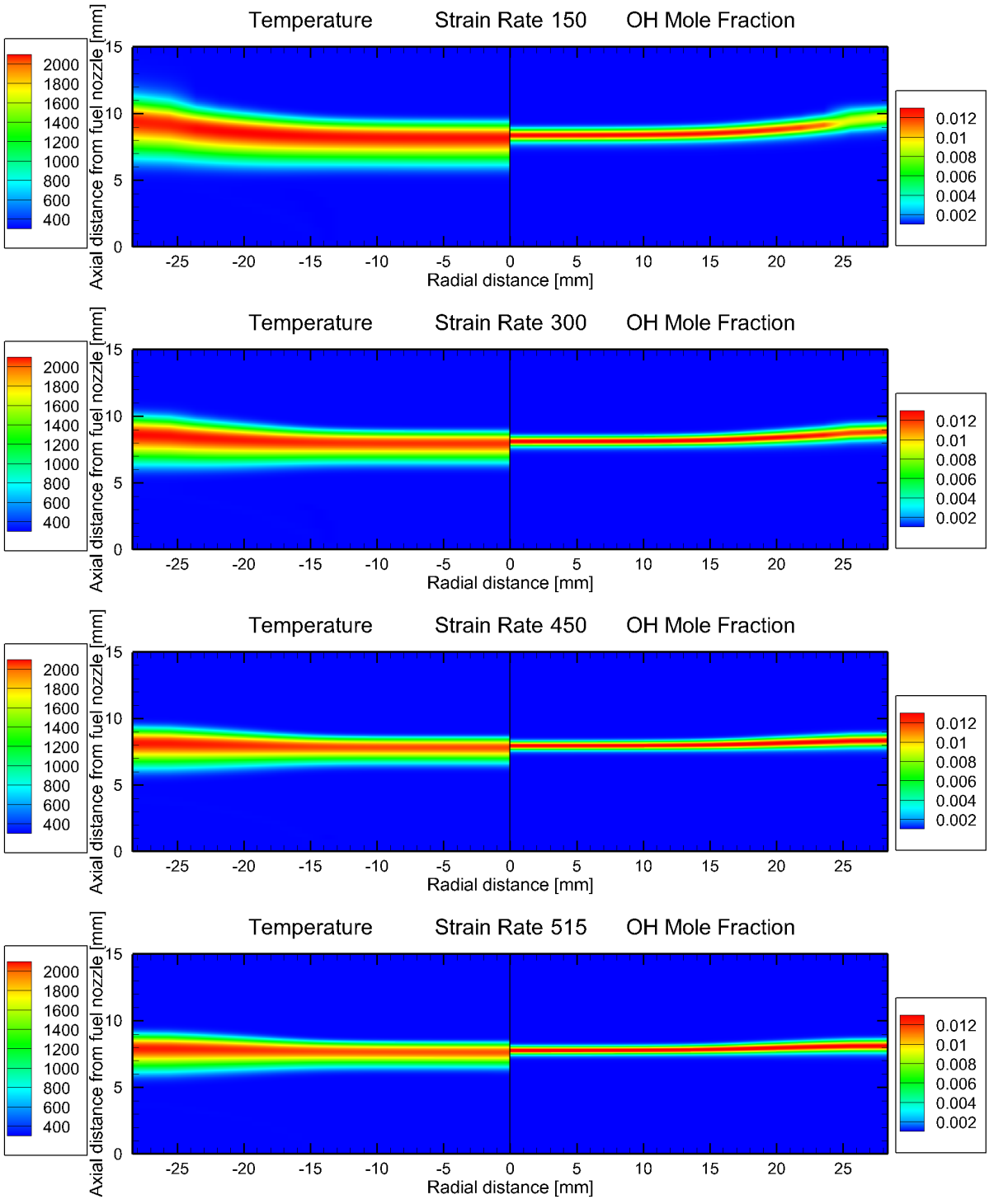

Figure 26: Temperature [K] and OH mole fraction contours for flames established at different global strain rates.

Figure 27 presents the mixture fraction and scalar dissipation rate contours for the same four flames. The flame is essentially composed of a thin reacting layer, embedded between two chemically inert external zones. As the strain rate increases, the scalar dissipation rate χ increases, causing an increase of heat conduction and reactant diffusion to the reacting zone. When χ exceeds a critical value, χ_q, incomplete reactions occur and heat loss from the flame is not balanced by heat release from chemical reactions. Consequently, the flame is extinguished [3]. In addition, the χ contours indicate that the higher scalar dissipation rate region is located near the axis of symmetry. Consequently, the local extinction is initiated in this region and then spreads radially out.

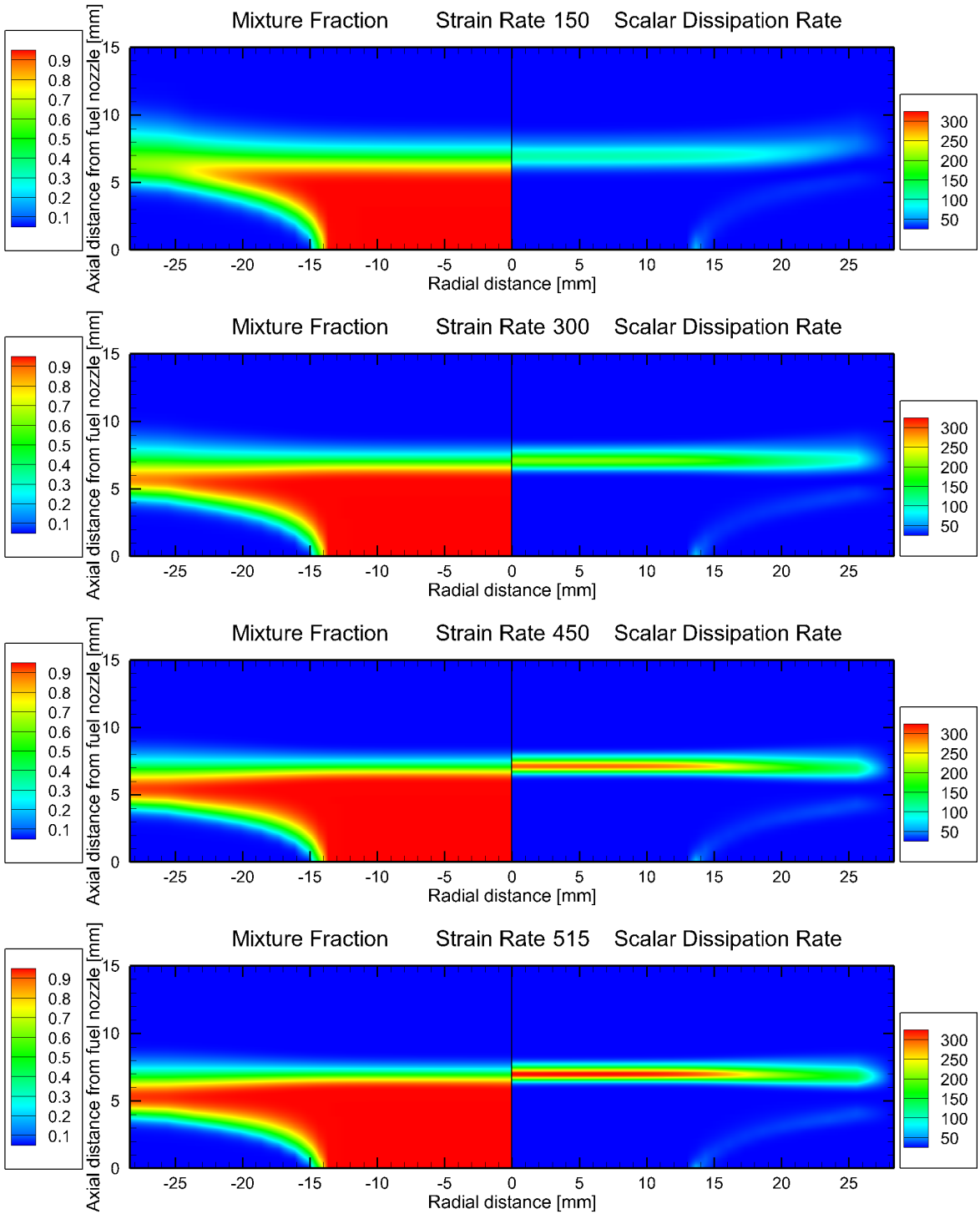

Figure 27: Diffusion flame structure in terms of mixture fraction and scalar dissipation rate contours at different strain rates.

Figure 28 plots the scalar dissipation rate profiles long the central line at different strain rates. As expected, the scalar dissipation rate increases and its critical value (χ_q) at extinction is 328 s-1 for the present case.

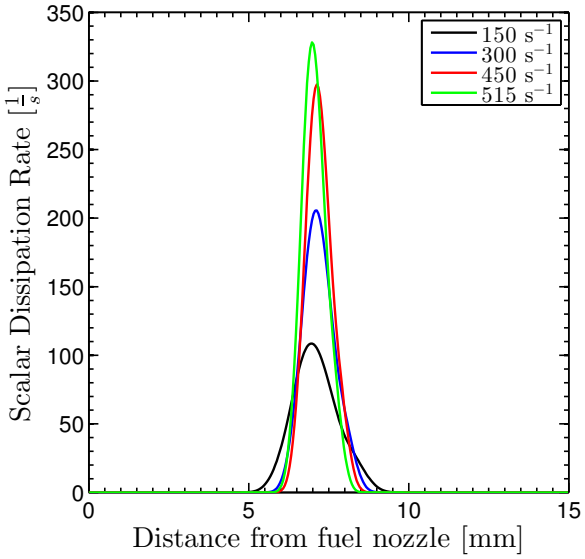

Figure 28: Scalar dissipation rate profiles along the centerline at different strain rates.

The stretch-induced extinction was also investigated using the 1-D computational model with CHEMKIN. Figure 29 compares the 1-D and 2-D results in terms of the scalar dissipation rate profiles for a moderately stretched flame (strain rate = 150 s^{-1}) and a flame near extinction (strain rate = 515 s^{-1}). Results clearly indicate the validity of 1-D predictions. For the highly stretched flame, the profiles match quite well except that the peak value is slightly higher for the

1-D case, while for the moderately stretched flame, the peak values match, but their locations are slightly different.

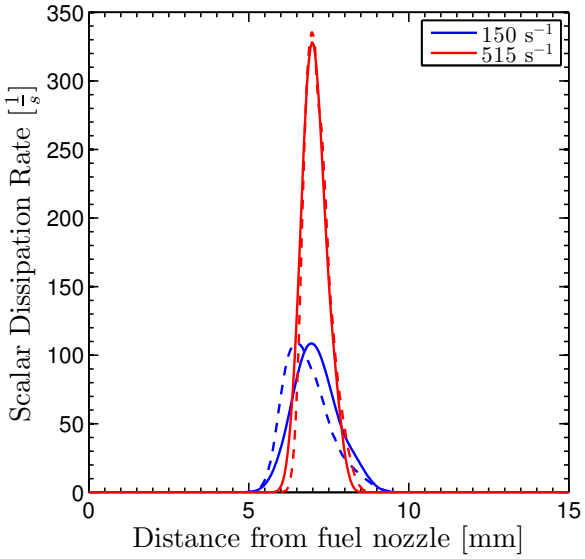

Figure 29: Comparison of the scalar dissipation rate profiles for 1-D and 2-D simulations. Solid lines indicate 2-D results.

6.3 Dilution-Induced Extinction

Results here focus on the dilution-induced extinction of diffusion flames. Simulations were performed by decreasing the O_2 mole fraction in the oxidizer stream until the flame extinguished. Figure 30 compares the 1-D and 2-D results in terms of the peak temperature plotted as a function of O_2 mole fraction for moderately and highly stretched flames at strain rates of 150 s^{-1} and 500 s^{-1} respectively. Consistent with previous results, there is good agreement between 1-D and 2-D predictions, except for slightly lower temperature for the latter case. There is also good agreement with respect to extinction conditions. For both 1-D and 2-D simulations, the minimum O_2 mole fractions at extinction are 7% and 9% for strain rates of 150 s^{-1} and 500 s^{-1}, respectively.

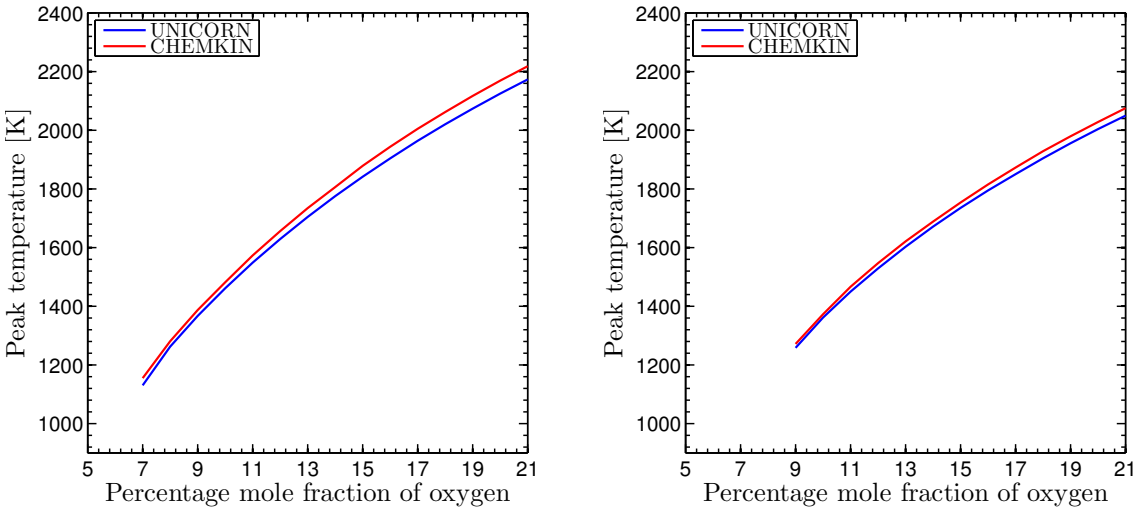

(a) (b)

Figure 30: Variation of peak flame temperature with O_2 mole fraction in the oxidizer stream, showing dilution-induced extinction for 1-D and 2-D simulations. Strain rates are 150 s^{-1} (a) and 500 s^{-1} (b).

Figure 31 depicts the flame structure and extinction process in terms of temperature and OH mole fraction contours for different O_2 mole fractions in the oxidizer. The strain rate is 150 s^{-1}. As the oxidizer stream dilution is increased by decreasing the O_2 mole fraction, the flame extinction is indicated by a continuous decrease in OH and temperature peaks, and by the thinning of reaction zone until extinction, which occurs at 7% O_2 mole fraction.

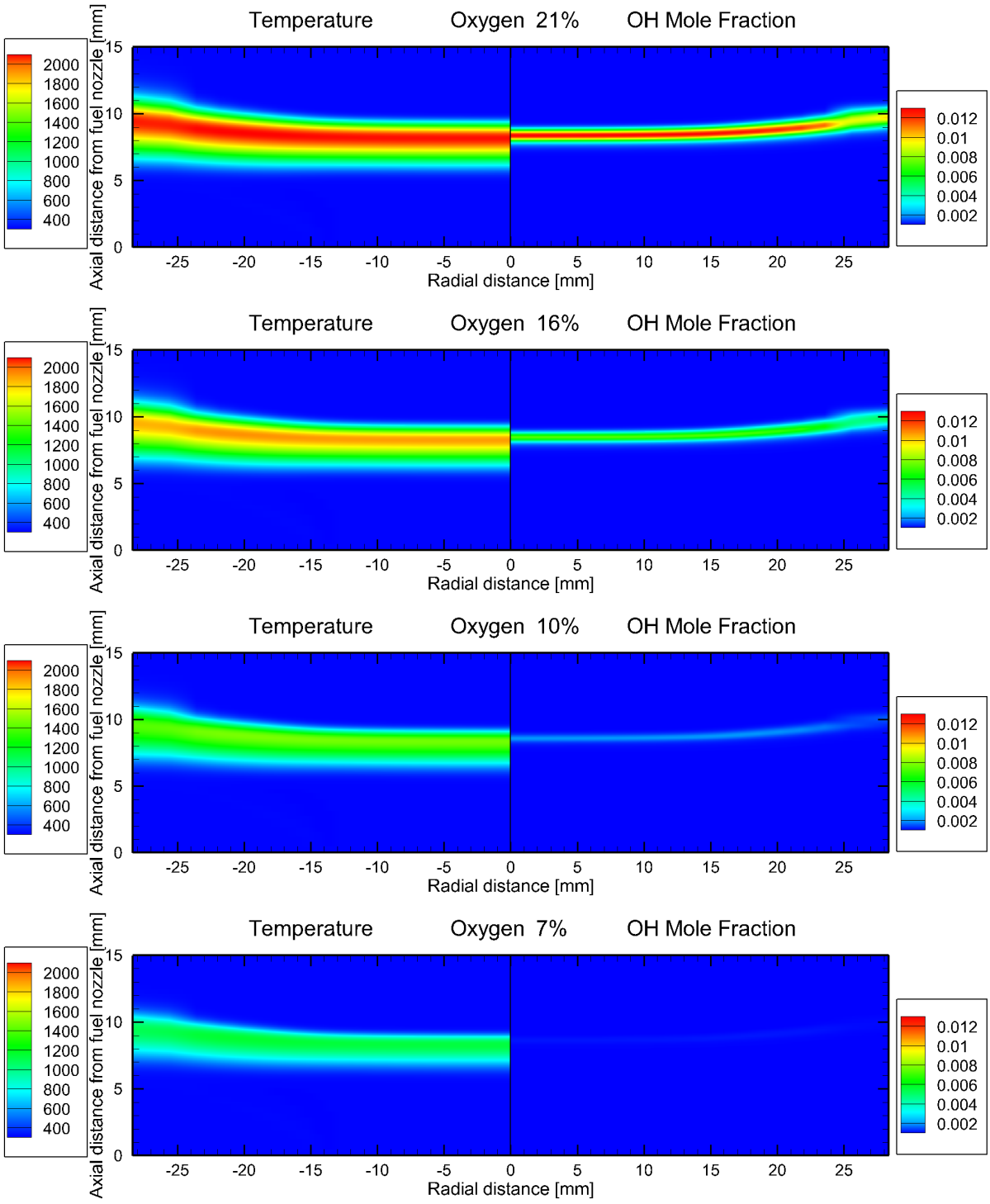

Figure 31: Temperature [K] and OH mole fraction contours for flames with different O_2 mole fractions in the oxidizer. Strain rate: 150 s^{-1}.

The validity of 1-D approach for predicting the dilution induced extinction is assessed by comparing the 1-D and 2-D results in terms of the scalar dissipation rate profiles presented in Figure 32. Here the results refer to the condition near extinction ($X_{O_2} = 0.07$). There is good agreement between the 1-D and 2-D profiles, except that the peak scalar dissipation rate for the 2-D case is higher by about 8% compared to the 1-D case.

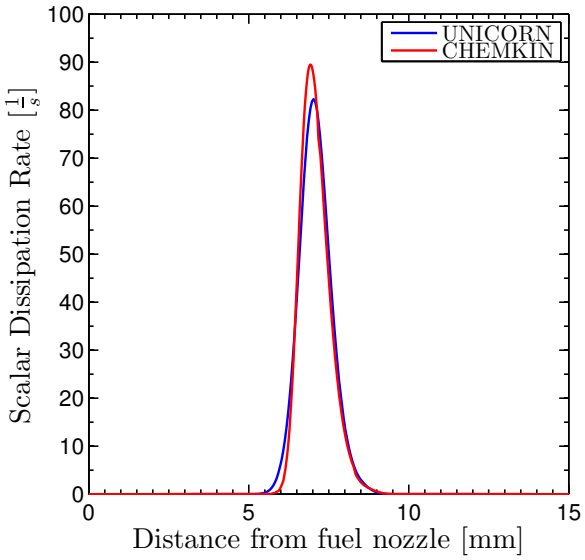

Figure 32: Comparison of the scalar dissipation rate profiles obtained with one- and two-dimensional simulations.

The 2-D results can be used to provide more details about the spatial and temporal behavior of the extinction process. For instance, the local extinction location can be identified by the location of the maximum scalar dissipation rate. Figure 33 plots the axial scalar dissipation rate profiles at four specific radial locations. The peak of the scalar dissipation rate is located along the central line and 7 mm from the fuel nozzle, indicating that the flame extinction is initiated at this location.

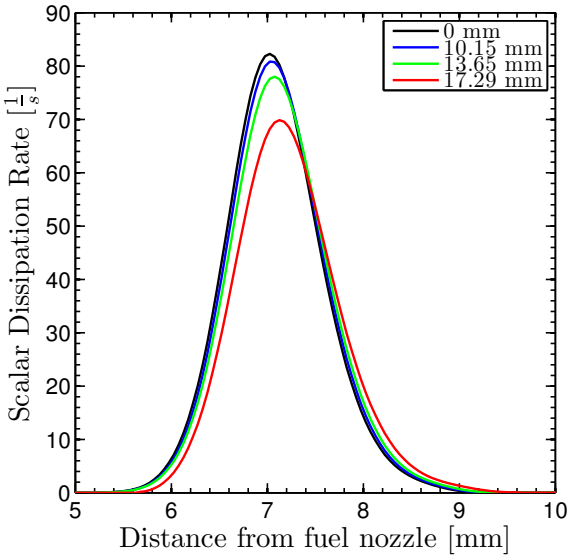

Figure 33: Scalar dissipation rate at different locations.

The temporal behavior of the extinction process can be examined by following the evolution of OH distribution in the flame. Figure 34 and Figure 35 present temperature, OH mole fraction and scalar dissipation rate contours at different times during the extinction process. For these simulations, the strain rate is 150 s^{-1} and O_2 mole fraction is 0.06. Note that for O_2 mole fraction = 0.07, the 2-D simulations predict a steady-state flame that is close to extinction. The comparison of OH contours at different times indicates that that flame extinction starts near the centerline where the scalar dissipation rate (χ) is the maximum. Further as indicated by OH contours at 1.75, 1.875, and 2.0 ms, the extinction proceeds rather quickly as the extinguished region spreads out radially.

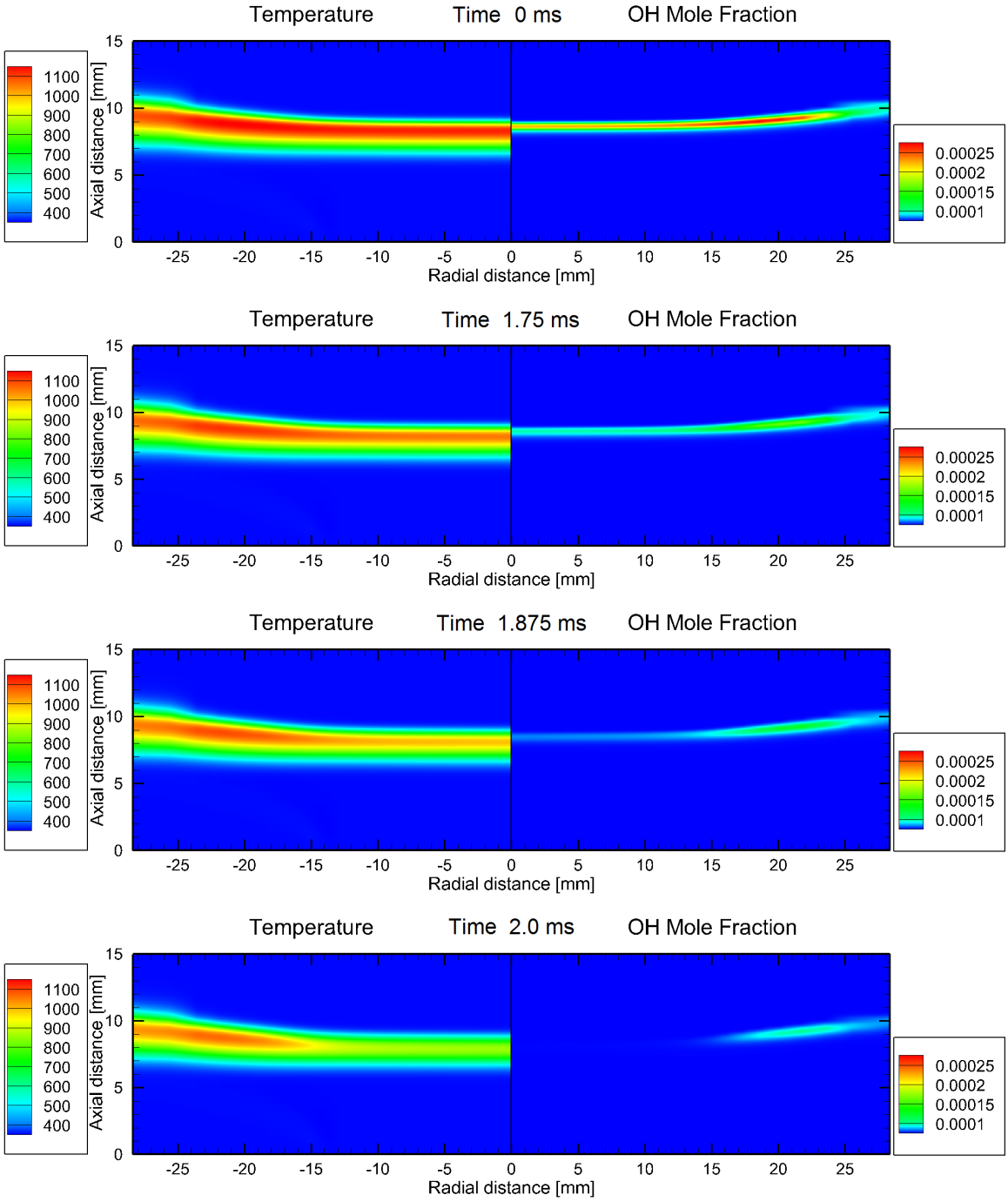

Figure 34: Flame extinction process depicted in terms of the temporal evolution of temperature and OH mole fraction contours. $X_{O_2} = 0.06$ and strain rate = 150 s^{-1}.

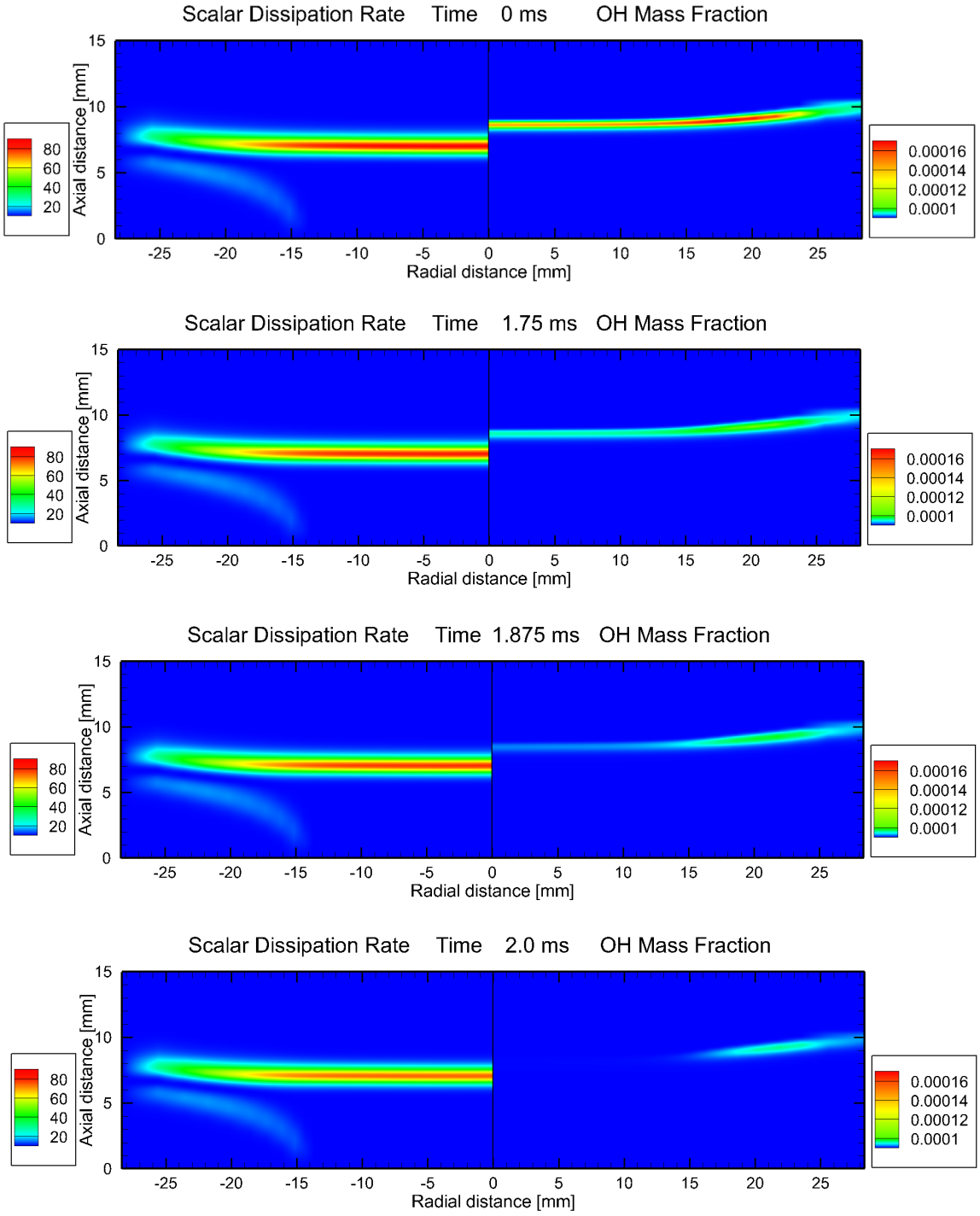

Figure 35: Flame extinction process depicted in terms of the temporal evolution of scalar dissipation rate and OH mass fraction contours. $X_{O_2} = 0.06$ and strain rate = 150 s^{-1}.

To further examine the diffusion flame structure, Figure 36 presents the the profiles of important major and minor species with respect to the mixture fraction ξ. Results are shown for both 1-D and 2-D simulations. In order to examine the similitude between the flame structures computed from 1-D and 2-D simulations, state relationships are plotted along the centerline. Two conditions are considered. One with strain rate equal to 150 s^{-1} and $X_{O_2} = 0.21$ represents a flame far from extinction, and the other with strain rate equal to 150 s^{-1} and $X_{O_2} = 0.07$ represents a flame near extinction. Note that $\xi = 1$ and $\xi = 0$ represent the fuel and oxidizer sides, respectively. Also $\xi_s = 0.179$ and 0.069 for the two flames simulated (Equation 6.6). The scalar plots represent a typical diffusion flame structure for both X_{O_2} cases. The fuel species (H_2 and CO) are completely consumed on the fuel side, while O_2 is consumed on the oxidizer side. The major product species H_2O and CO_2 attain their peak values near ξ_s. Moreover, the plots clearly indicate the similitude between the 1-D and 2-D simulations even for flames near extinction.

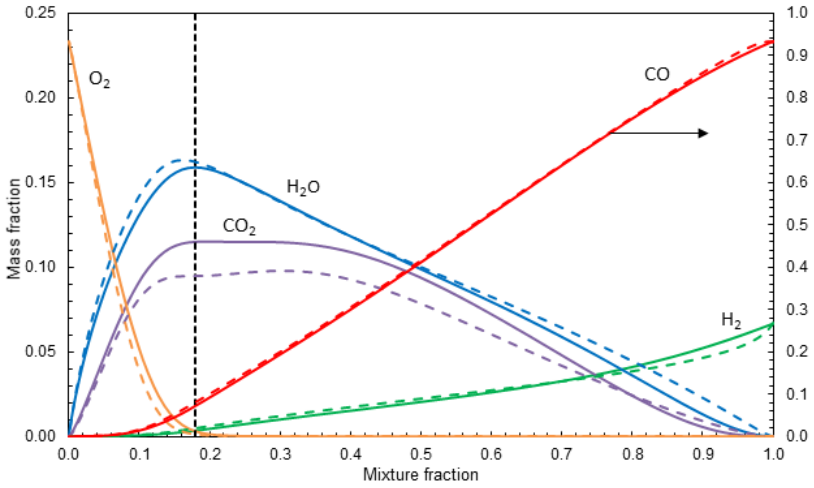

(a)

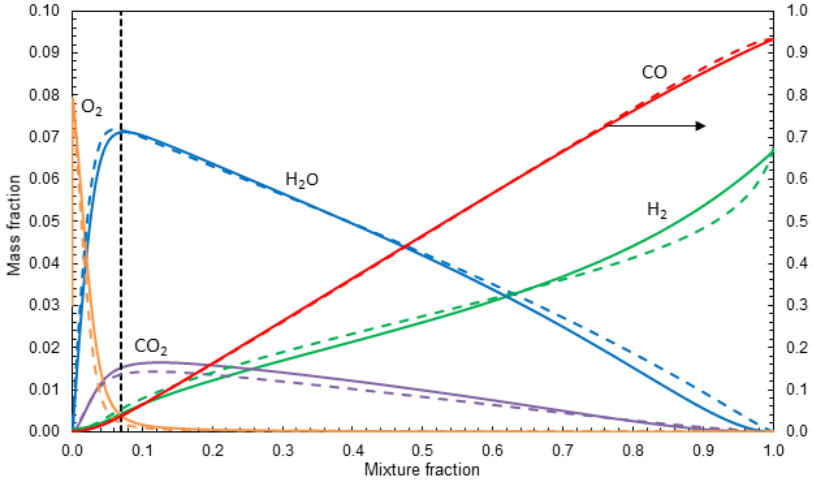

(b)

Figure 36: State relationships in terms of species profiles plotted with respect to two diffusion flames at X_{O_2} = 0.21 and 0.07 (near extinction). The strain rate = 15- s^{-1}. Vertical lines correspond to the stoichiometric mixture fractions. Results are shown for both 1-D and 2-D (solid lines) simulations.

CHAPTER 7

CONCLUSION

A comprehensive analysis about a low-energy-content fuel has been performed in the first part of the thesis. The exhaust stream of a solid oxide fuel cell stack contains CO_2, H_2O and some trace amount of H_2 and CO, resulting from incomplete utilization of fuel in the SOFC stack. The main objective of this section is discussing the possibility of extracting part of the retained energy content from the exhaust stream, investigating also the pollutant emissions deriving from the combustion process. Two initial temperatures for the fuel stream have been considered: 700 °C, which is equal to the outlet condition of the SOFC, and 970 °C, a higher temperature that would require a preheating of the incoming stream.

A preliminary study of the equilibrium composition shows that at equilibrium H_2 and CO are most consumed in the first case, when fuel inlet temperature is lower. In addition, the very high temperature of the second situation caused a greater production of NO_X compounds, making the first configuration the most suitable for real combustion processes. The effects of a change in equivalence ratio have been studied. The equivalence ratio strongly affects not only the equilibrium composition of the mixture, but also the adiabatic flame temperature by acting on the heat of combustion and heat capacity.

The study continued with the investigation of counterflow diffusion flames. A comparison between the two considered set ups is provided in terms of temperature, heat release rate profiles and mole fraction of the involved species. This further analysis confirmed that a temperature

of 700 °C is more than enough to provide an effective combustion process, whereas an increase in initial temperature does not give any advantage for either the integrated heat release rate or the production of pollutant compounds. For these reasons, this solution has to be discarded for conventional combustion processes.

The performances of the employed low energy fuel have been further discussed. The flammability limits have been evaluated in terms of dilution of the oxidizer. Keeping the imposed strain rate fixed to 150 s^{-1}, the system requires a minimum mole fraction of O_2 in the oxidizer equal to 10% to reach a steady state laminar diffusion flame. Staring from the minimum allowable percentage of oxygen up to 100%, the evolutions of peak temperature, peak heat release rate and integrated heat release rate show a similar growing trend, reaching their maxima for oxy-combustion. The influence of the dilution of the oxidizer on mole fractions of the most relevant species have been studied. To conclude this part, an interesting analysis about the extinction behavior of counterflow flames is provided. In particular, the flammability boundaries are evaluated for the involved fuel mixture. As the strain rate increases, the required minimum percentage of oxygen in the oxidizer mixture is computed, until blow off extinction is reached. The flammability boundary constructed with strain rate and O_2 percentage in the oxidizer presents the expected growing trend, showing that increasing the stretching of the flame, a higher content of oxygen in the oxidizer becomes necessary to ignite and obtain a steady state diffusion flame. Moreover, we found that for a wide range of strain rate values, combustion can occur when air is employed as oxidizer. Thanks to these data, we understand that this fuel mixture can be used in wide range of initial conditions. Therefore, inside this interval of

values, the flame could withstand a kinetic adjustment without the occurrence of extinction. For this reason, this kind of study is very important to evaluate the suitability of this fuel in real applications.

In the second part of the work, UNICORN multidimensional CFD code is employed to study counterflow diffusion flames. After a brief review of the combustion characteristics of the earlier analyzed fuel mixture, the main focus shifted to the extinction behavior of flames fueled by a common mixture of syngas (50% H_2 - 50% CO). Throughout the whole investigation, special attention is paid to the comparison of the results obtained with one- and two-dimensional simulations. As matter of fact, one of the principal objectives of this part is to evaluate the goodness of the one-dimensional assumption usually made when counterflow flames are analyzed. Setting up a moderately stretched flame, the thermal and chemical profiles obtained with both one- and two-dimensional codes, show that the outputs match very well. Afterwards, the flammability limits due to blow off are computed and resulted in a small mismatch between one- and two-dimensional simulations. The influence of the increase in strain rate on the peak temperature is reported, constructing a diagram of peak temperature as function of the imposed strain rate. Plotting the contours surfaces of temperature and OH mole fraction gives the possibility to visualize the effects of a change in stretching on the structure of the flame. As we increase the velocities of fuel and oxidizer the reacting zone becomes more narrow and the maximum temperature drops. When studying the flammability limits, nonequilibrium effects becomes dominant in the physics of the phenomenon. For this reason, to effectively describe the extinction behavior of a flame it is decisive to analyze the evolution of the scalar dissipation

rate. The results very well predicted the location and condition in which the flame starts to extinguish, proving that, also for syngas flames, the scalar dissipation rate is a powerful tool in the study of flame extinction behavior. Again, along with the output data given by UNICORN code, the simulations have been repeated using CHEMKIN and the results have been compared. While for high strain rate the scalar dissipation rate profiles matched very well, for moderately stretched flames, the curve representing the one-dimensional data is slightly shifted to the fuel side.

In the last section of the work, dilution-induced extinction is covered. The mole fraction of oxygen in the oxidizer mixture is reduced until steady state flame is no longer obtained. Two configurations were taken into accounts: moderately and highly stretched flames. In both case, CHEMKIN and UNICORN predicted equal flammability limits and the results in terms of peak temperature at different O_2 content well matched. Study about the scalar dissipation rate was also performed, showing a good outcome in the prediction of location of beginning of extinction and in the matching between one- and two-dimensional outputs.

In conclusion, the exploitation of the retained energy inside the exhaust gas of solid oxide fuel cell stack may represent a feasible way to increase the total efficiency of the system, as part of the energy coming from the retained reacting compounds (H_2 and CO) inside the mixture can be recovered. When dealing with conventional combustion processes (no catalysis involved), the best solution is maintaining the same outlet condition of the SOFC stack. This way the heat production is greater, the pollution impact is lower and no external energy is required to carry out the combustion process.

Furthermore, thanks to the use of UNICORN code and the study of the scalar dissipation rate, a detailed investigation of the extinction behavior of syngas counterflow flames has been carried out. Comparing the results obtained with one- and two-dimensional simulations, we can assert that in general the one-dimensional assumption made for counterflow flame problems is reasonable for syngas fuels, since in most of the analyses the outputs matched very well. The knowledge of flammability limits and extinction behaviors are of great importance from a purely scientific point of view, but most of all they provide solid information about the best conditions in which a fuel has to be employed.

CITED LITERATURE

1. Beychok, M. R.: Process and environmental technology for producing SNG and liquid fuels. U.S. EPA report EPA-660/2-75-011, May 1975.

2. Jewulski, J., Kupecki, J., Tenerowicz, P., Swiatkowski, B., Kuczynski, P., Stefanski, M., and Razum, M.: Solid oxide fuel cell combined cooling, heating and power with poly-fuel: Operation and maintenance. SOFCOM, WP3, Project n 278798, May 2013.

3. Chen, R. and Axelbaum, R. L.: Scalar dissipation rate at extinction and the effects of oxygen-enriched combustion. Combustion and Flame, 142:62–71, 2005.

4. Appleby, A. J. and Foulker, F. R.: Fuel Cell Handbook. New York, Van Norstand Reinhold, 1989.

5. Katta, V. R., Aggarwal, S. K., and Roquemore, W. M.: Evaluation of chemical-kinetics models for n-heptane combustion using a multidimensional CFD code. Fuel, 93:339–350, 2012.

6. CHEMKIN. Reaction design, Retrieved October 2013, from http://www.reactiondesign.com/products/chemkin/chemkin-2.

7. Katta, V. R., Hu, S., Wang, P., Pitz, R. W., Roquemore, W. M., and Gord, J. R.: Investigations on double-state behavior of the counterflow premixed flame system. Proceedings of the Combustion Institute, 31:1055–1066, 2007.

8. Katta, V. R., Meyer, T. R., Brown, M. S., Gord, J. R., and Roquemore, W. M.: Extinction criterion for unsteady, opposing-jet diffusion flames. Combustion and Flame, 137:198–221, 2004.

9. Shih, H. Y., Hsu, J. R., and Lin, Y. H.: Computed flammability limits of opposed-jet H_2/CO syngas diffusion flames. International Journal of Hydrogen Energy, 39:3459–3468, January 2014.

10. Solid Oxide Fuel Cells. US department of energy page on SOFCs, Retrieved October 2013, from http://energy.gov/fe/science-innovation/clean-coal-research/solid-oxide-fuel-cells.

11. Quesito, F.: Modeling and Experimental Analysis of Biogas in Diesel and Solid Oxide Fuel Cell Generators. Tesi di laurea, Politecnico di Torino, University of Illinois at Chicago, 2011/2012.

12. Cipriani, F.: Numerical Analysis of Use of Syngas for Combustion Systems and in Solid Oxide Fuel Cells. Tesi di laurea, Politecnico di Torino, University of Illinois at Chicago, 2012/2013.

13. Jockenhvel, T., Schneider, R., Sandell, M., and Schlter, L.: Optimal power plant integration of post-combustion CO_2 capture. Siemens AG, Energy Sector, 2009.

14. CHEMKIN Overview. Sandia web site, Retrieved November 19, 2013, from http://public.ca.sandia.gov/chemkin.

15. March, J.: Advanced Organic Chemistry: Reactions, Mechanisms, and Structure. New York, Wiley, 1985.

16. Chemical-Kinetic Mechanisms for Combustion Applications. San Diego Mechanism web page, Mechanical and Aerospace Engineering (Combustion Research), University of California at San Diego, Retrieved October 2013, from http://combustion.ucsd.edu.

17. Som, S., Ramírez, A., Hagerdorn, J., Saveliev, A., and Aggarwal, S.: A numerical and experimental study of counterflow syngas flames at different pressures. Fuel, 87:319–334, June 2007.

18. Davis, S., Joshi, A., Wang, H., and Egolfopoulos, F.: An optimized kinetic model of H_2/CO combustion. Proceeding of Combustion Institute, 30:1283–1292, 2005.

19. Metcalfe, W. K., Burke, S. M., Ahmed, S. S., and Curran, H. J.: A hierarchical and comparative kinetic modeling study of C_1–C_2 hydrocarbon and oxygenated fuels. International Journal of Chemical Kinetics, 45:638–675, August 2013.

20. Smith, J. P., Golden, D. M., Frenklach, M., Moriarty, N. W., Eiteneer, B., Goldenberg, M., Bowman, C. T., Hanson, R. K., Song, S., Gardiner, W. C., Lissianski, V. V., and Qin, Z.: . Master's thesis, http://www.me.berkeley.edu/gri_mech/.

21. Berta, P., Aggarwal, S. K., and Puri, I. K.: An experimental and numerical investigation of n-heptane/air counterflow partially premixed flames and emission of no_x and PAH species. Combust Flame, 145:740–64, 2006.

22. Turns, S.: An Introduction to Combustion, Concepts and Applications. McGraw-Hill, 2012.

23. Warnatz, J., Mass, U., and Dibble, R. W.: Combustion. Verlag, Berlin, Heidelberg, New York, Springer, 1996.

24. CHEMKIN Theory Manual. Reaction Design.

25. Reynolds, W.: The Element Potential Method for Chemical Equilibrium Analysis: Implementation in the Interactive Program Stanjan. Department of Mechanical Engineering Stanford University, 1986.

26. Law, C. K., Makino, A., and Lu, T. F.: On the off-stoichiometric peaking of adiabatic flame temperature. Combustion and Flame, 145:808–819, 2006.

27. Kee, R. J., Miller., J. A., and Evans, G. H.: Proceedings of the twenty-second symposium (international) on combustion. The Combustion Institute, page 1479, 1988.

28. Karman, T. V. and Angew, A.: Uber laminare and turbulente reibung. Math. Mech., 1:233, 1921.

29. Schlichting, H.: Boundary Layer Theory. New York, McGraw-Hill, 1979.

30. Evans, G. H. and Greif, R.: Numerical Heat Transfer, volume 14. 1988.

31. Shih, H. Y. and Hsu, J. R.: A computational study of combustion and extinction of opposed-jet syngas diffusion flames. International Journal of Chemical Kinetics, 36:15868–15879, 2011.

32. Jaluria, Y.: Computer Methods for Engineering with MATLAB Applications. Taylor & Francis, 2011.

33. T'ien, J. S.: Diffusion flame extinction at small stretch rates: the mechanism of radiative loss. Combustion and Flame, 65:31–34, 1986.

34. Annon.: Computational Submodels. International workshop on measurement and computation of turbulent nonpremixed flames, 2001, http://www.ca.sandia.gov/TNF/radiation.

35. Katta, V. R., Goss, L. P., and Roquemore, W. M.: Numerical investigations of transitional H_2/N_2 jet diffusion flames. AIAA J, 32:84, 1994.

36. Katta, V. R. and Roquemore, W. M.: Calculation of multidimensional flames using large chemical kinetics. AIAA, 46:1640–50, 2008.

37. Briones, A. M., Aggarwal, S. K., and Katta, V. R.: Effects of H_2 enrichment on the propagation characteristics of CH_4air triple flames. Combustion and Flame, 153:367–383, 2008.

38. Tecplot. Master's thesis, Retrieved April 2014, from www.tecplot.com.

39. Chelliah, H. K., Law, C. K., Ueda, T., Smooke, M. D., and Williams, F. A.: An experimental and theoretical investigation of the dilution, pressure and flow-field effects in the extinction conditions of methane air diffusion flames. Proc. Combust. Inst., 23:503–511, 1990.

40. Katta, V. R., Hu, S., Wang, P., Pitz, R. W., Roquemore, W. M., and Gord, J. R.: Investigation of double-state behavior of the counterflow premixed flame system. Proc. Combust. Inst., 31:1055–1066, 2007.

41. Mahallawy, F. E. and Habik, S. E. D.: Fundamentals and Technology of Combustion. Elsevier, 2002.

42. Kulander, J. L.: Departures from the Saha equation in an optically thin nitrogen gas. Journal of Quantitative Spectroscopy and Radiative Transfer, 5:253–269, 1965.

VITA

NAME Daniele Bongiovanni

EDUCATION B.Sc., Mechanical Engineering, Politecnico di Torino, Italy, 2012

M.Sc., Mechanical Engineering, Politecnico di Torino, Italy, 2014

M.Sc., Mechanical Engineering, University of Illinois at Chicago, 2014

HONORS TOP-UIC mobility scholarship for Double Degree program, 2013-2014

Full scholarship issued by "Fondazione Ferrero Onlus", 2010-2014

SECAC mobility scholarship for Bachelor Exchange program between Politecnico di Torino and Louisiana State University, 2011